Wayne State University Theses

January 2020

Characterization, Modeling, And Thermal Management Of High-Performance Lithium Batteries

Minjun Bae
Wayne State University

CHARACTERIZATION, MODELING, AND THERMAL MANAGEMENT OF HIGH-PERFORMANCE LITHIUM BATTERIES

by

MINJUN BAE

THESIS

Submitted to the Graduate School

of Wayne State University,

Detroit, Michigan

in partial fulfillment of the requirements

for the degree of

MASTER OF SCIENCE

2020

MAJOR: MECHANICAL ENGINEERING

Approved By:

_____
Advisor   Date

_____
Co-advisor   Date

DEDICATION

This thesis is dedicated to my family whom I love the most in the world.

ACKNOWLEDGEMENTS

TABLE OF CONTENTS

LIST OF TABLES

LIST OF FIGURES

CHAPTER 1. BACKGROUND AND MOTIVATIONS OF RESEARCH

1.1)   Lithium-ion Batteries: State-of-the-art

A battery is a device that stores electrical energy in the form of chemical energy. There are two types of batteries: primary and secondary batteries. Primary batteries are non-rechargeable batteries, such as alkaline batteries and zinc-carbon batteries, while secondary batteries are rechargeable batteries, such as lithium-ion (Li-ion) batteries, lead-acid (PbA) batteries, nickel metal hydride (NiMH) batteries, and nickel cadmium (NiCd) batteries. Among these secondary batteries, Li-ion batteries have been attracting much attention as a power source in the past few decades. They are dominantly used in portable electronic devices, such as laptops, cell phones, and digital cameras due to high energy density, excellent cyclability, low weight, and no memory effect. A conventional Li-ion battery cell consists of four major components: negative and positive electrodes, referred to as anode and cathode, respectively, a separator, and an electrolyte. The electrochemical performance of a Li-ion battery cell is mainly determined by electrochemical reactions between two electrode materials. These two electrodes are connected to an external electrical supply, but physically separated by a separator, which enables the free ionic flux through its microporous structure. An electrolyte used in commercially available Li-ion batteries is typically a mixture of organic carbonates that contain lithium (Li) ions. The basic operational principle of a Li-ion battery is illustrated in Figure 1. During the discharging process, the electrons are forced to be released at the anode and move to the cathode through the external load. Simultaneously, Li ions internally move in the same direction, from the anode to the cathode, via the electrolyte. In this way, the external energy is electrochemically stored in the battery cell in the form of the chemical energy. During the charging process, the opposite
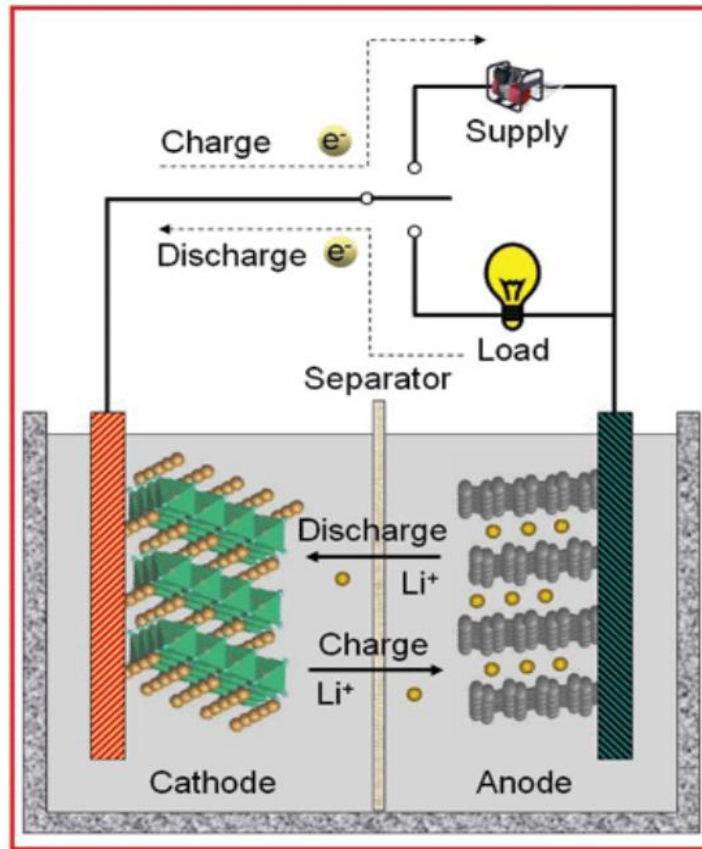
Figure 1. Schematic illustration to show the basic components and the operation principle of a Li-ion battery. Reproduced with permission [1].

happens.

For anode active materials, graphitic carbons are dominantly used in commercial Li-ion batteries owing to their layered structure, which facilitates Li intercalation and deintercalation. However, the maximum theoretical capacity of the graphitic anodes is 372 mAh/g, which is not sufficient to meet the requirements of future energy storage applications. For cathode active materials, $LiFePO_4$ and $LiCoO_2$ are widely used. $LiCoO_2$ is characterized by its facile large production and stability under ambient conditions. However, $LiCoO_2$ experiences significant structural changes and capacity fade induced by a series of phase transitions at charging voltages

greater than 4.2 V, lowering its practical capacity to ~140 mAh/g [2]. Moreover, the issues of high material cost and toxicity of the $LiCoO_2$ still remain unsolved. Using $LiFePO_4$ as a cathode active material provides benefits of the improved stability, cyclability, temperature tolerance (−20 °C to 70 °C), and environmental benignity. Nevertheless, due to the crystal structure of $LiFePO_4$, which is characterized by one-dimensional channels along [010] direction, impurities can be easily stuck in the channels and interrupt the diffusion of Li ions.

Electrolytes should be electrochemically stable in an operating voltage and temperature ranges with the ability to sufficiently form a passivation layer with two electrodes without degradation or decomposition. Electrolytes used in commercial Li-ion batteries are mostly mixtures of alkyl carbonates owing to several features, such as low toxicity and relatively wide temperature and voltage ranges. The alkyl carbonates include ethylene, dimethyl, diethyl and ethyl-methyl carbonates (EC, DMC, DEC, EMC, respectively), and $LiPF_6$ is used as a salt [3]. The selection of electrolyte solutions should be carefully made with consideration of safety features, operating temperature ranges, the electrochemical stability, and the ability to transport ionic charge carriers. Besides liquid electrolytes, solid-state electrolytes, solid-state electrolytes, and gel polymer electrolytes (GPEs) have gained much attention because these types of electrolytes can effectively mitigate undesirable Li dendritic growth for Li metal batteries. The Li dendritic growth is specifically discussed in Chapter 2. Specific features of these electrolytes are not covered in this thesis, but have been reviewed and discussed elsewhere [3-9].

A separator must be appropriately selected with consideration of their essential properties clarified below:

1) Sufficient porosity to absorb a liquid electrolyte for high ionic conductivity

2) Uniformly distributed pores that are smaller than particle sizes of electrode components to achieve a uniform charge distribution

3) Uniform permeability that does not significantly increase the electrical resistance

4) Ample wettability to retain electrolytes

5) High mechanical robustness to withstand high pressure during the battery assembly

Since these features are typically in a trade-off relationship, the trade-off should be well adjusted depending on an application. Separators can be typically classified into three types:

1) Microporous membranes

2) Non-woven fabric mats

3) Inorganic composite membranes

Most of the microporous membranes, which are dominantly used in the commercial Li-ion batteries, are based on semi-crystalline polyolefin materials, such as polyethylene (PE), polypropylene (PE), their blends, and high-density PE [10]. Microporous polyolefin membranes are characterized by their thinness and thermal shutdown operation. For the thermal shutdown operation, membranes with a different boiling point are multi-layered. If one layer starts melting, the melted membrane fills the pores of other membranes, efficiently shutting down further ionic transport. A non-woven separator is a fibrous mat synthesized by chemically, physically, or mechanically combining numerous fibers. Non-woven separators are often featured by their high mechanical robustness, which allows them to be utilized as a supporting framework for GPEs [11]. Inorganic composite separators, often referred to as ceramic separators, are a porous mat composed of inorganic nanoparticles bonded with a binder, typically polyvinylidene fluoride-co-hexafluoropropylene (PVDF-HFP). These separators show an exceptional wettability with all

5

non-aqueous liquid electrolytes due to their high hydrophilicity and tremendous surface area provided by inorganic nanoparticles. Moreover, inorganic composite separators show a substantial thermal stability that is a favorable characteristic for large-scale Li-ion battery applications, such as battery electric vehicles (BEVs).

Despite the high electrochemical performance of Li-ion batteries, the limited theoretical capacity of commercially used graphitic anodes hinders the utilization of Li-ion batteries for newly emerging energy storage applications. Intensive research efforts have been made in search of an alternative anode material to develop higher-energy-density batteries. Among various potential candidates, Li metal has been considered as one of the most promising alternative anode materials. However, the problematic Li dendritic growth during the discharging process and the infinite volume expansion resulted from the host-less nature of the Li metal hinder the commercialization of the Li metal anode. In Chapter 2, the fundamentals of Li metal dendritic growth and common research strategies to tackle down this issue are discussed.

1.2) Scope of this Thesis

This thesis is written with an objective to provide general and advanced knowledge of Li-based energy storages. Not only are nano-scale strategies to improve the electrochemical performance of Li-ion batteries included, but system-scale solutions for efficient and safe Li-ion battery operation are included in this thesis. Discussion starts from designs of nanomaterials to enhance the performance of a Li-ion battery cell and moves on to the systematic solutions to achieve stable thermal behavior of large-scale Li-ion batteries.

CHAPTER 2. BEYOND LITHIUM-ION BATTERIES: LITHIUM METAL BATTERIES

Li metal is considered as a promising anode material due to its superior specific capacity (3860 mAh/g), and the lowest electrochemical potential (-3.040 V versus standard hydrogen electrode) [12-18]. Li metal is also a very favorable anode material for beyond Li-ion batteries, such as Li-Sulfur and Li-Air batteries. However, the undesirable Li dendritic growth hampers practical applications of the Li metal, causing severe safety concerns and poor cycling behavior. During Li plating, the discharging process, a solid electrolyte interface (SEI) layer spontaneously forms onto the surface of the Li metal due to the highly reactive nature of Li metal. To be specific, in case of commercially available Li-ion batteries in which organic carbonates are used as an electrolyte, the initial SEI layer is mainly the product of Li alkyl carbonates (ROCOOLi) as a result of one electron reduction reaction. These ROCOOLi can be further converted to Li_2CO_3 with a trace amount of water. Depending on electrolytes used, Li_2O and Li halides can be also present in the SEI layer [20]. Since the electrochemical properties of each component is different, the SEI layer shows inhomogeneity in composition: inner layer is dominated by relatively stable components, such as Li_2CO_3, Li_2O, Li halides, while metastable ROCOOLi tend to be located at the outer layer [21-22]. Due to the inhomogeneity of the composition, the SEI layer exhibits inhomogeneous conductivity, which eventually leads to heterogeneous Li electrodeposition. As a result, volumetric fluctuations induced by the host-less nature of the Li metal are accelerated at particular sites, introducing curves and kinks on the SEI layer. Since the SEI layer is not mechanically rigid enough to withstand the infinite volume expansion of the Li metal, cracks form onto the SEI layer, exposing fresh Li underneath. The exposed fresh Li becomes preferential Li nucleation sites due to its low energy barrier, further accelerating local Li dendritic growth [23-24]. Furthermore, unlike the flat SEI surface, the dendritic protrusions
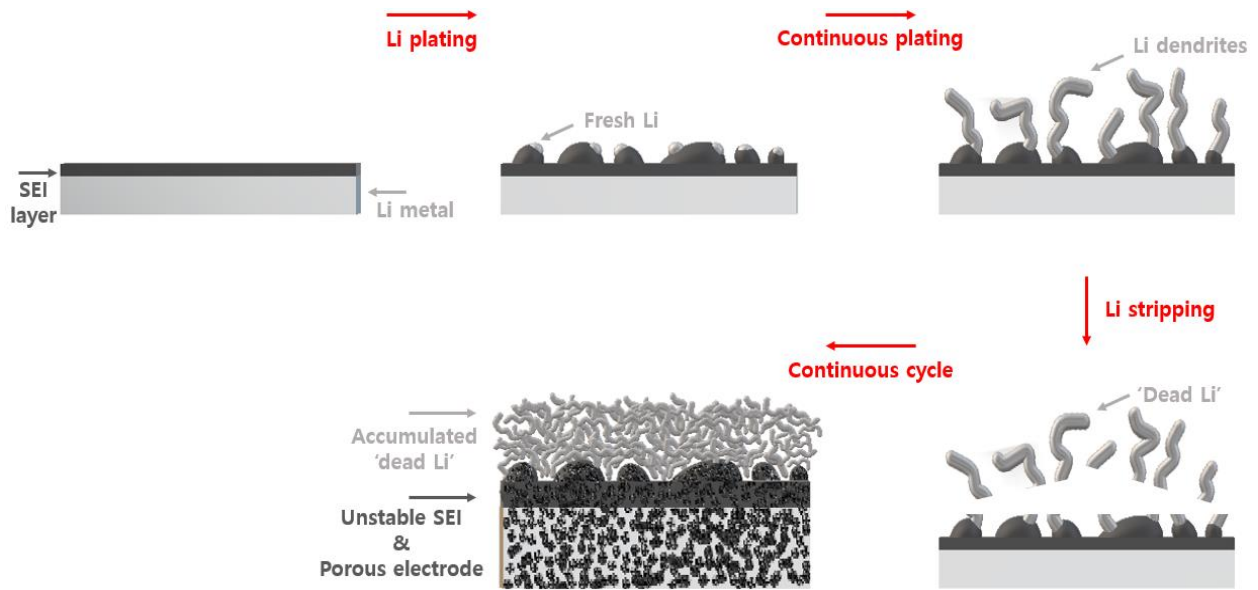
Figure 2. Schematic illustration of Li plating process on the Li metal. As Li plating proceeds, cracks formed in the SEI layer by volumetric fluctuations of Li expose fresh Li underneath. Li dendrites further grow as Li plating continues. Mechanically fragile Li dendrites become isolated during Li plating. Continuous cycling eventually results in a thick and unstable SEI with the porous electrode underneath.

enable the three-dimensional Li-ion diffusion, leading to faster Li dendritic growth. The existence of Li dendrites can damage the separator by penetration. This causes the electric short circuit, which could potentially lead to thermal runaway and cell explosion. Moreover, Li dendrites get destroyed during Li stripping, the charging process, because of their physical fragility. As a result, the broken Li dendrites, often referred to as dead Li, are accumulated on the SEI layer, increasing the interfacial resistance [25-26]. Continuous cycling results in an unstable and thick SEI layer with the accumulated dead Li on the surface, eventually leading to a failure of a battery cell. The step-by-step Li dendritic growth is illustrated in Figure 2. Despite a tremendous amount of research work to understand the fundamentals of Li dendritic growth, the exact mechanism remains elusive due to its highly complex nature. To obtain a deeper insight

into the principles of the Li dendrite formation, researchers have devoted to theoretical investigations by numerical simulations. In Chapter 3, the phase-field method, which is a powerful tool to study highly non-linear microstructural evolutions, is introduced. Moreover, a two-dimensional Li electrodeposition model developed by Ely et al. [48] is introduced to obtain a deeper grasp of formulation of the phase field method.

CHAPTER 3. THEORETICAL INVESTIGATIONS ON LITHIUM DENDRITIC GROWTH

3.1) The Phase Field Method

Although many experimental studies on the fundamentals of Li dendritic growth have provided valuable contributions, theoretical studies are often preferred due to the highly complex mechanism of Li dendritic growth, which is influenced by many internal and external factors, for example, structure and composition of the SEI layer, and the electrolyte used, the nucleus-substrate contact angle, the current density, and so on. Among various theoretical approaches, a phase-field model (PFM) has been attracting much attention as a versatile tool to study structural changes of materials. One of the biggest advantages of the PFM is the utilization of the diffuse interface model. Although the sharp interface model conventionally used in free boundary problems, such as phase transformations and microstructural evolutions, can be efficient to study the evolution of simple microstructural geometries, it induces a discontinuity into the simulation model due to the difficulty of tracking a moving interface. In contrast, the diffuse interface model used in the PFM avoids this issue by continuous variations of an order parameter, often referred to as phase-field variable (Figure 3). The continuity obtained from this approach captures the position of the interfaces by values of the phase-field variables, and thus provides the predictability of complex and arbitrary microstructural evolutions. In the PFM, the governing equations of the microstructural evolution are represented by means of a set of partial differential equations expressed by the phase-field variables, which are functions of time and spatial coordinates. There are two types of phase-field variables: non-conserved and conserved variables. The evolution of the non-conserved variables is determined by the Allen-Cahn equation, which
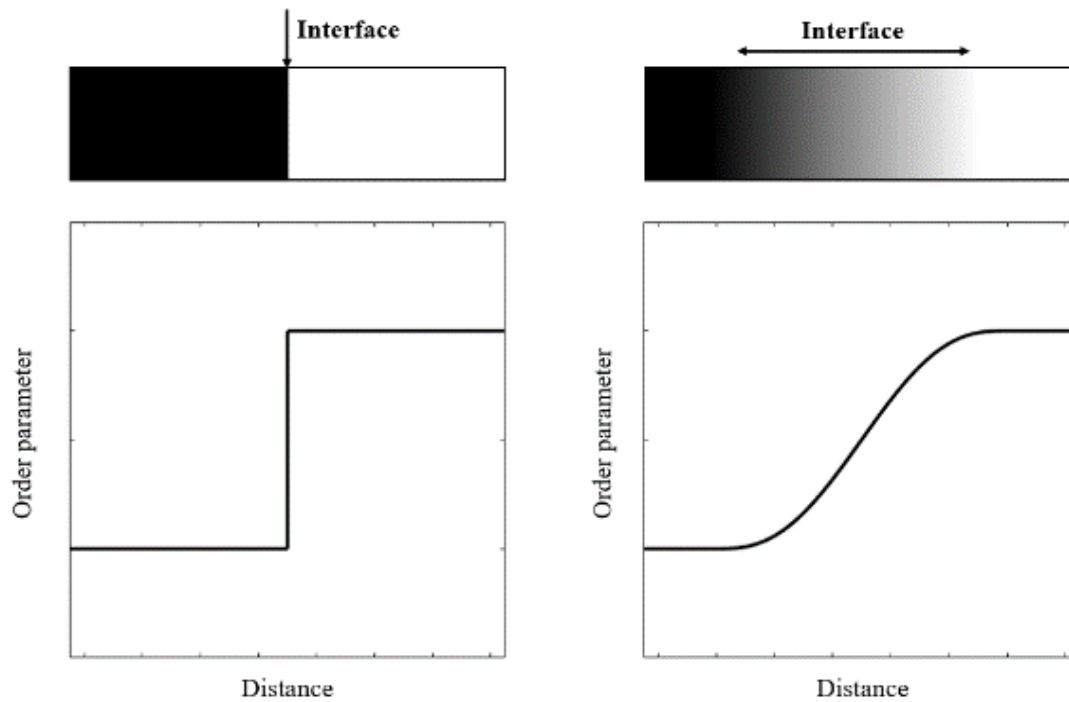
Figure 3. The sharp interface (left) and the diffuse interface (right) models.

describes the microstructural evolution. The evolution of the locally conserved variables is determined by the Cahn-Hilliard equation, which contains the information of the local charge distribution. Since the equations that represent the evolution of the phase-field variables are derived based on general thermodynamic and kinetic principles, the kinetics of individual atoms are not explicitly included. As a result, empirical parameters of material properties should be included in the simulation [27]. The enhanced computer technology has allowed for the intensive development of the PFMs to investigate 1) solidification [28-33], 2) precipitation [34-38], 3) epitaxial growth [39-40], 4) electromigration [41-42], and 5) solid-state sintering [43-44]. The PFMs have also been applied to a vast range of electrochemical phenomena. Guyer et al. [45-46] developed the first one-dimensional electrochemical PFM that describes equilibrium and kinetic behaviors of electrochemistry. The inspiration was obtained from the physical analogy between

the governing equations of solidification and electrodeposition dynamics: analogies between 1) the varying overpotentials of the electrochemistry and the supercooling of the alloy solidification, 2) the interfaces of solid-melt and electrode-electrolyte, and 3) the dendrite formation during the solidification and the electrodeposition.

Among various electrochemical PFMs, Li electrodeposition models have been intensively studied to investigate the fundamentals of the undesirable Li dendritic growth dynamics. The first PFM of the electrodeposition was proposed by Shibuta et al. [47] by coupling two different driving forces: an electrostatic potential described by the Cahn-Hilliard equation and a thermodynamic potential formulated from a variation of the Ginzburg-Landau free energy functional. In their work, the morphological evolution driven by the electrodeposition of copper as functions of the applied voltage and concentration of the copper ion was successfully simulated. Ely et al. [48] presented a PFM of Li electrodeposits, which includes the contribution of the heterogeneous nucleation energy to the free energy of transformation of the system by the implementation of the contact angle. Chen et al. [49] introduced a thermodynamically consistent PFM that accounts for the non-linear nature of Li dendritic patterns. Recently, Yurkiv et al. [50] closely monitored the effect of the SEI layer and the anisotropic diffusion behavior of Li ions on Li dendritic growth. In their work, both filamentous and mossy Li dendritic growth were explicitly visualized in the simulation results by including the contributions of the elastic deformation energy to the free energy transformation of the system. In the following section, a PFM from Ely et al. [48] is introduced to provide a deeper understanding of formulations of the PFM. To avoid confusion, same symbols are used as presented in the paper.

3.2) Framework & Formulations

The total Gibbs free energy of transformation, ΔG_T, for an isothermal, isobaric system is defined as:

$$\Delta G_T[\xi, \rho; P, T] = \int_V [\Delta g_v \, p(\xi) + \rho\phi] \, dV + \int_V \left[W_\xi g(\xi) + \frac{\varepsilon_\xi^2}{2} |\nabla \xi|^2] dV \right] dV \tag{1}$$

$$+ \int_A Z(\xi) dA$$

where Δg_v is the empirical volumetric free energy of the transformation, ξ is the non-conserved phase field variable, which is equal to zero in the liquid (electrolyte) phase and one in the solid (deposited lithium on the electrode) phase. ρ is the charge density expressed as:

$$\rho \equiv F \sum_{j=1}^{n} z_j C_j \tag{2}$$

where F is the Faraday's constant, z_j is the valence and C_j is the mole per volume concentration. The subscript j represents the number of electrochemical components in the system. ϕ is the electrostatic potential, ε_ξ^2 is the gradient energy coefficient, which penalizes interfaces that are too narrow, $p(\xi)$ is an interpolating function that needs to be implemented due to the multi-phase nature of the system. The interpolating function, $p(\xi)$, is typically designed to be simple for an efficient numerical simulation. $g(\xi)$ is the double well function that determines the equilibrium profile and the interfacial energy. Figure 4 shows the graphs of $p(\xi)$ and $g(\xi)$, which are expressed as:

$$p(\xi) = \xi^3 (6\xi^2 - 15\xi + 10) \tag{3}$$
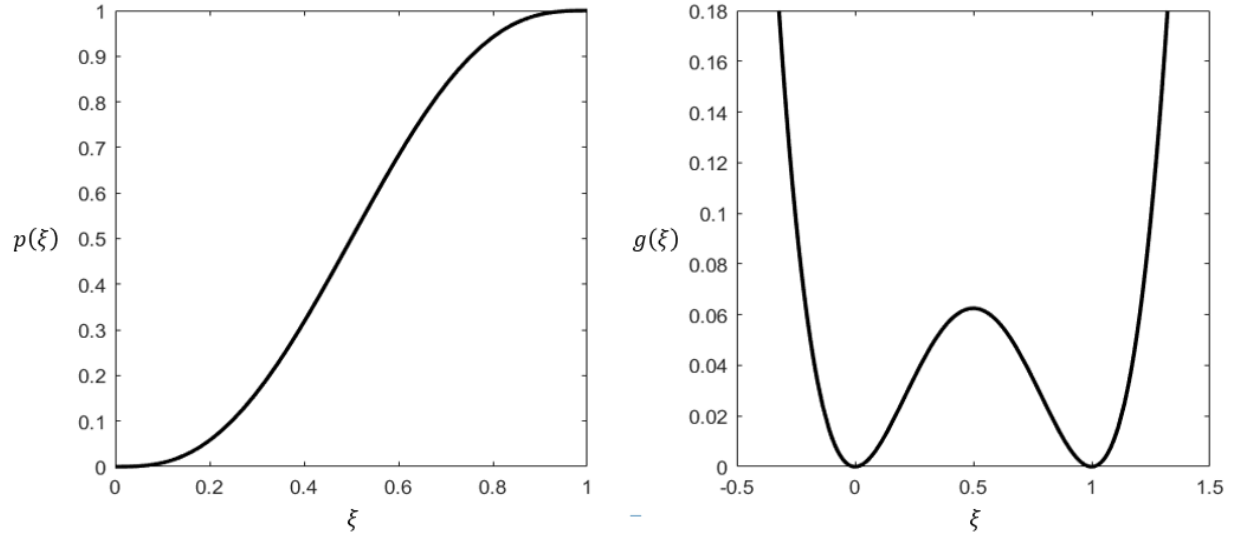
Figure 4. The interpolating function (left) and double well function (right) plots. It is clearly shown that $p(0) = 0, p(1) = 1, p'(0) = p'(1) = 0$ and $g(0) = g(1) = 0, g'(0) = g'(1) = 0$.

$$g(\xi) = \xi^2(1 - \xi)^2 \tag{4}$$

where W_ξ is the energy barrier of the double well function, which penalizes interfaces that are too broad. $Z(\xi)$ is the work of adhesion imposed by the contact angle between a substrate and a lithium nucleus, and A is the interfacial surface boundary. The local equilibrium is then given by:

$$\frac{\delta \Delta G_T}{\delta \xi} = \Delta g_v \frac{\partial p(\xi)}{\partial \xi} + W_\xi \frac{\partial g(\xi)}{\partial \xi} - \varepsilon_\xi^2 \nabla^2 \xi = 0 \tag{5}$$

$$\frac{\delta \Delta G_T}{\delta \rho} = \phi = \phi_0 \tag{6}$$

with the surficial boundary condition on A:

$$\hat{n} \cdot \nabla \xi = cos\theta * \xi_0(1 - \xi_0) * \left(\sqrt{2}\delta_\xi\right)^{-1} \tag{7}$$

phase field value at the substrate, θ is the contact angle between a substrate and a lithium nucleus,

and $\hat{n}$ is the unit normal vector. Equation 5 and 6 indicate the spatial uniformity of voltage of the system and the balance between the surface tension and the chemical free energy driving force. Away from the equilibrium state, the value of Equation 5 becomes non-zero, and the electrostatic potential of Equation 6, which is a function of the interfacial gradient of the composition, shifts. Therefore, the time-dependent phase evolution governed by the locally non-conserved phase field variable, ξ, is described by the Allen-Cahn equation:

$$\frac{\partial \xi}{\partial t} = -M_\xi \left(\frac{\delta \Delta G_T}{\delta \xi}\right) - \dot{\psi}\left(\nabla\xi, \frac{\delta \Delta G_T}{\delta \xi}, \frac{\delta \Delta G_T}{\delta \rho}\right) \tag{8}$$

where $\dot{\psi} = \dot{\psi}\left(\nabla\xi, \frac{\delta \Delta G_T}{\delta \xi}, \frac{\delta \Delta G_T}{\delta \rho}\right)$ is the interfacial plating rate, which is only active at the SEI in the numerical simulation. M_ξ is the phase field mobility that specifies the rate of change during the electrodeposition. In case of no plating, Equation 8 should reduce to the classic Allen-Cahn equation. In this case, according to Boettinger and Warren [29]:

$$\varepsilon_\xi^2 = 6\gamma_{NE}\delta_\xi \tag{9}$$

$$W_\xi = 3\gamma_{NE}/\delta_\xi \tag{10}$$

where γ_{NE} is the interfacial energy between the lithium nucleus and the electrolyte. Fundamentally, an increase in γ_{NE} will induce an increase in θ as well as the energy height, W_ξ. Similarly, $\frac{\partial \xi}{\partial t}$ is replaced by $-v\frac{\partial \xi}{\partial x}$, where v is the normal velocity, in case of the homogeneous electrodeposition in which the contact angle, θ, is zero. For small variances away from the equilibrium state, $\vec{v} \cdot \nabla\xi = \dot{\psi}$. As a result, the evolution of the non-conserved phase field variable, ξ, is described by Equation 11:

$$\frac{\partial \xi}{\partial t} = -M_\xi \left(\Delta g_v \frac{\partial p(\xi)}{\partial \xi} + W_\xi \frac{\partial g(\xi)}{\partial \xi} - \varepsilon_\xi^2 \nabla^2 \xi \right) + \Omega \vec{\Gamma} \cdot \nabla \xi \tag{11}$$

where Ω is the solid-phase lithium molar volume. The electrodeposition rate $\vec{\Gamma}$ is described by the Butler-Volmer equation with modifications:

$$\vec{\Gamma} = j_0 (e^{(1-\alpha)K} - e^{-\alpha K}) \hat{n} \tag{12}$$

$$K = \frac{zF\eta}{RT} + \frac{\gamma_{NE} k \Omega}{RT} \tag{13}$$

$$k = -\nabla \cdot (\nabla \xi / |\nabla \xi|) \tag{14}$$

where j_0 is the exchange current density, α is the charge transfer coefficient that describes the electrochemical kinetics of the system. η is the local overpotential, which is the shift in the potential difference across the interface, which causes current to pass, and k describes the curvature of the interface. The local overpotential is then defined as:

$$\eta = -\delta_\xi \hat{n} \cdot \nabla \frac{\delta \Delta G_T}{\delta \rho} = (\delta_\xi \hat{n}) \cdot (-\nabla \phi) \tag{15}$$

where $\hat{n} = \frac{\nabla \xi}{|\nabla \xi|}$ for $|\nabla \xi| \neq 0$, and zero otherwise. In case that current densities are smaller than the limiting current, $K \ll 1$, Equation 12 reduces to:

$$\vec{\Gamma} = j_0 K \hat{n} \tag{16}$$

where the flat interface velocity is defined as $v = \Omega \vec{\Gamma} \cdot \hat{n} = j_0 \Omega z F \eta / RT$. According to Boettinger and Warren [29], the phase mobility is then defined as:

$$M_\xi = -\frac{j_0 \Omega^2}{6\delta_\xi RT} \tag{17}$$

In analogy to Equation 11, the distribution of the locally conserved charge density, ρ, is determined by the Cahn-Hilliard equation:

$$\frac{\partial \rho}{\partial t} = \nabla \cdot M_\rho \nabla \frac{\delta \Delta G_T}{\delta \rho} + zF\Omega \vec{\Gamma} \cdot \nabla \xi = \nabla \cdot M_\rho \nabla \phi + zF\Omega \vec{\Gamma} \cdot \nabla \xi \tag{18}$$

where M_ρ is the electric conductivity defined as:

$$M_\rho = \sigma_\xi p(\xi) + \sigma_L (1 - p(\xi)) \tag{19}$$

where σ_ξ and σ_L are the electrical conductivity in the solid-lithium phase and the electrolyte phase, respectively.

Equations (11) to (19), which include the bulk electrochemical contribution term, the interfacial energy term, and the surface tension term, were then finally coupled to simulate two-dimensional Li dendritic growth. Simulation results indicate that Li nuclei larger than the critical size, $r > r^* = -\frac{2\gamma_{NE}}{\Delta g_v}$, where r is the radius, evolve in a way that follows their minimum energy configuration, while Li dendrites tend to shrink in case of Li nuclei being smaller than the critical size. The electric field exhibited the highest value in the vicinity of the dendrite tips, accelerating further Li dendritic growth. It is well known that Gibbs transformation energy decreases when the heterogeneous nucleation sites created by the substrate-nucleus contact angle, θ, are present [51-55]. The simulation results provide a deeper grasp of the dependency of Li dendrites on θ, suggesting that small values of θ result in high Coulombic efficiencies as well as a relatively uniform Li deposition throughout the substrate, while larger values of θ engage the local

evolution of Li dendrites, causing the ununiform distribution of the Li deposition. Such a theoretical approach can provide a great-depth insight into the fundamentals of Li dendrites, enabling researchers to conduct studies on the effects of various parameters on Li dendritic growth. Our ongoing research effort is to prove the functionality of various novel-structured nanomaterials to guide the uniform Li electrodeposition without Li dendrites by using the specified PFM with modifications. In the following section, strategies to mitigate the undesirable Li dendritic growth are proposed. Furthermore, I present porous metallic titanium (Ti) nanorods on a metal Ti substrate as a current collector for a dendrite-free lithium metal anode. The porous Ti nanorods successfully provided superior cell stability as well as outstanding Coulombic efficiencies, all of which were further confirmed by a series of electrochemical tests.

CHAPTER 4. TITANIUM NANORODS FOR A STABLE LITHIUM METAL ANODE

4.1) Introduction

Tremendous experimental research efforts have been made to circumvent the problematic Li dendritic growth. Major strategies include:

1) The introduction of electrolyte additives

2) Solid-state electrolytes

3) Artificial SEI coatings

4) Novel-structured current collectors

The SEI stabilization has been achieved by introducing electrolyte additives, such as fluoroethylene carbonates [56-57], Li polysulfides [58], vinylene carbonates [59], and even a trace amount of water [60]. These electrolyte additives actively react with Li and create a stable passive layer on the Li metal anode, contributing to the stabilization of the SEI layer. However, the lack of sustainability of these additives and the low mechanical robustness of the SEI layer are still hurdles to the complete suppression of Li dendritic growth. The solid-state electrolytes have also gained much attention due to their ability to physically suppress the Li dendrite formation [61-64]. Nevertheless, the limited ionic conductivity and increased interfacial impedance remain as challenges for meeting the desirable power requirements at ambient conditions. The protective SEI coating can effectively facilitate the uniform Li electrodeposition and avoid Li dendritic growth by preventing the physical contact between the Li metal anode and the electrolyte. However, they cannot address the infinite volume fluctuation of the Li metal during cycling, which is another major issue to overcome to commercialize the Li metal anode. Therefore, researchers have devoted to developing novel-structured current collectors to

efficiently guide the uniform Li deposition and minimize the volume expansion of the Li metal anode. For example, Zhao et al. [65] fabricated a 3D porous copper current collector via a novel linear sweep voltammetry electrochemical etching method and achieved an improvement in cyclability and stability of a half cell and a full cell. Liu et al. [66] developed a Li-coated porous polyimide matrix and successfully achieved low voltage hysteresis. Lin et al. [67] designed a layered Li-reduced graphene oxide composite, which exhibited excellent flexibility and small volume expansion during cycling, all of which contributed to the stabilization of the SEI layer. Although these materials have significantly expanded the scope of approaches to avoiding Li dendritic growth, the use of various materials in a fabrication process is not favorable in practical battery manufacturing processes. Herein, I introduce highly porous metallic Ti nanorods on a Ti substrate as a novel current collector that guides the uniform Li electrodeposition without Li dendrites. The metallic Ti nanorods are featured by several advantages as a Li metal current collector:

1) The presence of Ti provides high electrode conductivity

2) The high level of porosity facilitates Li electro-crystallization

3) Multi-directional nanorods arrays provide tremendous surface area

4) Mechanical robustness provided by high Young's modulus of Ti is favorable in a battery manufacturing process

Tremendously porous Ti nanorods provide numerous heterogeneous nucleation sites, attracting Li ions at the initial Li plating. After the initial Li nucleation, the lithiated Ti nanorods further engage Li electrodeposition on bodies of the nanorods, leading to the morphology I refer to 'fat-nanorods'. Figure 5 illustrates the Li plating process on a flat metal surface and Ti
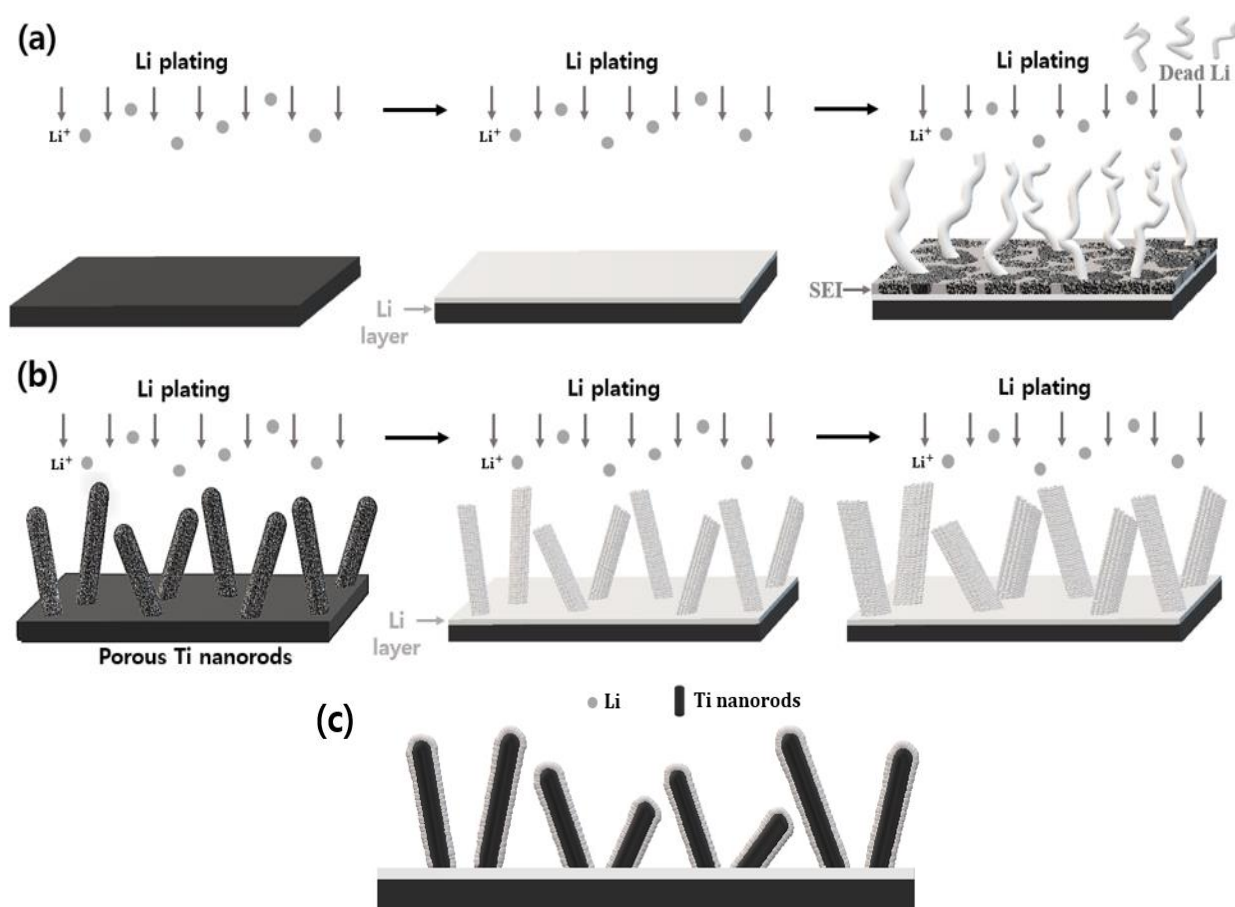
Figure 5. Schematic illustration of the Li plating process. (a) Li plating on a pure metal substrate: unstable SEI, dead Li, and Li dendrites are present. (b) Li plating on the porous Ti nanorods: Li preferentially deposits on Ti nanorods, further attracting lateral Li growth on the bodies of the nanorods due to low energy cost. The stabilization of SEI is achieved with no dendrites. (c) a cross-sectional view of the lithiated Ti nanorods.

nanorods. The lithiated Ti nanorods, as a dendrite-free Li metal anode, demonstrated its superior cell stability and cyclability, and the Coulombic efficiency, which remained 100 % over 1,400 cycles at a current density of 1 mA/cm^2 and a capacity of 1 mAh/cm^2. Moreover, other potential engineering applications of black metallic Ti covered with nanorod arrays are discussed.

4.2) Material Synthesis

Deng et al. [13] previously reported a simple fabrication method of porous Ti nanorods on a metallic Ti substrate. First, to grow TiO_2 nanorods on a metallic Ti substrate, the hydrothermal synthesis was employed with a NaOH solution (0.25 M) and a piece of metallic Ti foil (0.5 x 0.5 cm^2) as a mineralizer and a substrate, respectively. The hydrothermal synthesis is a powerful technique to prepare a variety of nano-structured materials, such as nanorods, nanowires, nanobelts, and so on. The main advantage of this technique is the controllability of nanostructures by simply adjusting a set temperature, reaction time, and the amount of an aqueous solution used for the reaction. A Teflon-lined autoclave was used as a reactor, which was heated to 220 °C. The reaction lasted for 24 hours, and the sample was then naturally cooled down to the room temperature. After the hydrothermal reaction, the sample was rinsed with deionized water, immersed in an HCl solution (0.6 M) for 1 hour to exchange Na ions with protons, rinsed with deionized water again, and dried under the ambient conditions. The samples were then calcinated at 600 °C for 2 hours with the presence of the air. After the calcination, as shown in Figure 6, TiO_2 nanorods were successfully grown on a metallic Ti substrate. It should be noted that the physical properties of the TiO_2 nanorods vary with the amount of the mineralizer, NaOH, and its concentration. It has been widely confirmed that the percent of filling level of the solvent affects the vapor pressure above the liquid phase boundary. Moreover, small variances from the targeted concentration of the NaOH solution, which is 0.6 M, can affect the kinetics of crystal growth: a low concentration of the NaOH solution can increase the growth rate of crystal faces (Figure 6b). Since the optimization of material properties is not the focus, TiO_2 nanorods with a greater thickness (Figure 6a) were simply used for experiments to obtain more surface area and better visualization for the morphology study discussed in the next section.
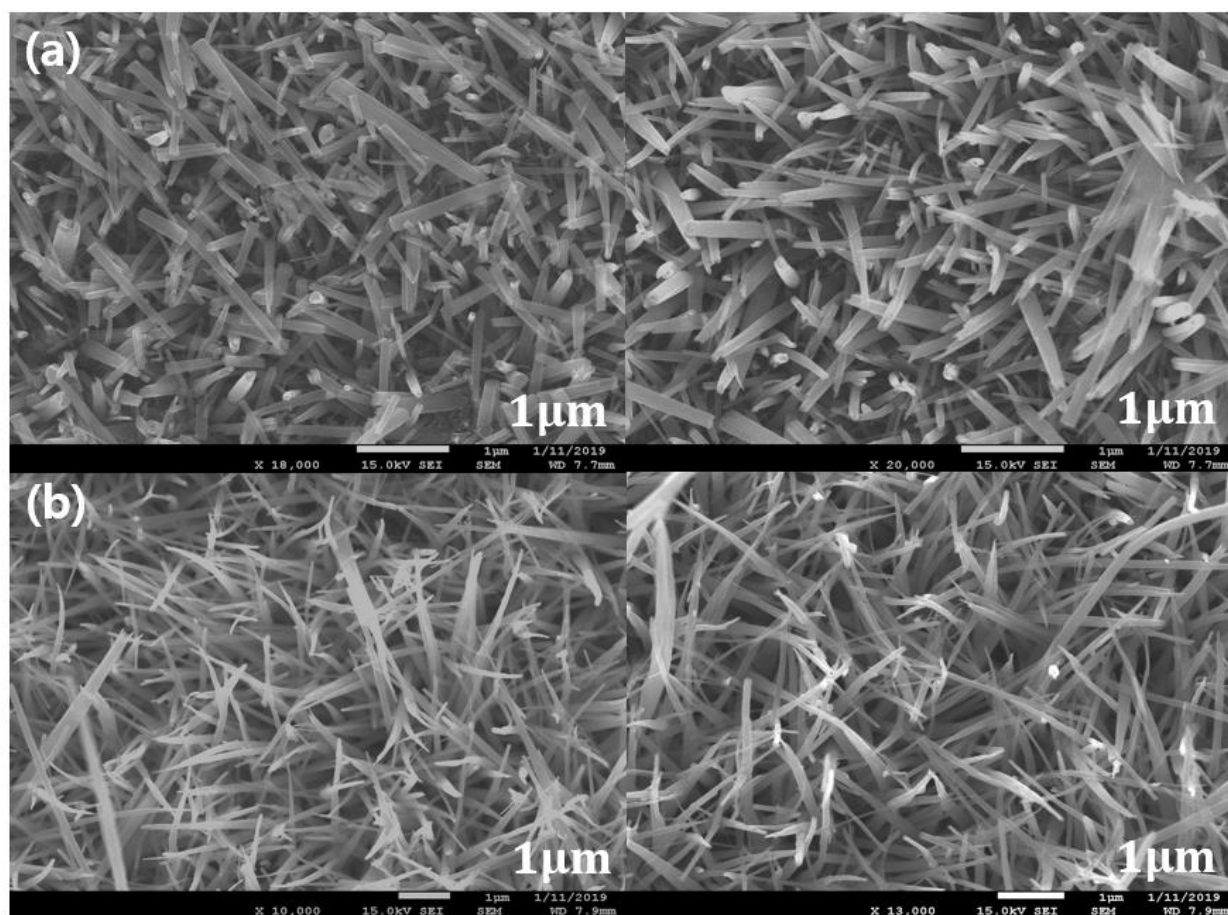
Figure 6. Morphologies of the TiO$_2$ nanorods on a metallic Ti substrate. (a) TiO$_2$ nanorods and (b) TiO$_2$ nano-needles.
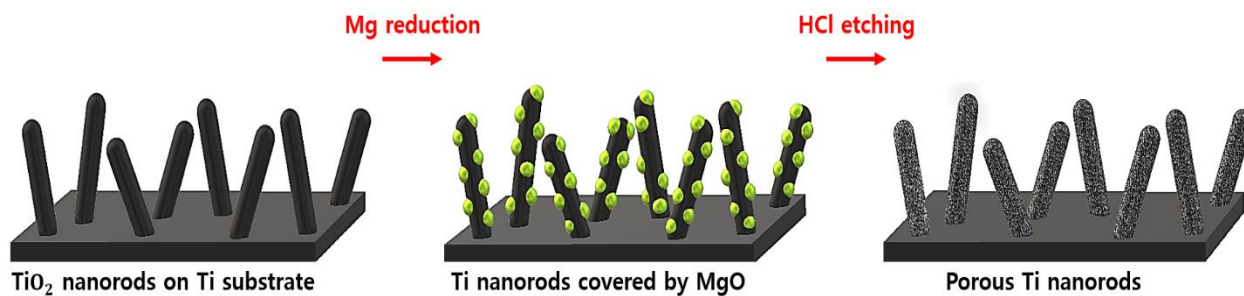
Figure 7. Schematic illustration of the magnesiothermic reduction of TiO$_2$ nanorods.

Figure 7 explains the magnesiothermic reduction of TiO$_2$ nanorods. The sample was completely covered with 25 mg of magnesium (Mg) powder inside a clean crucible, which was put into a tube furnace. The crucible was then heated to 650 °C in 1 hour and maintained at the set
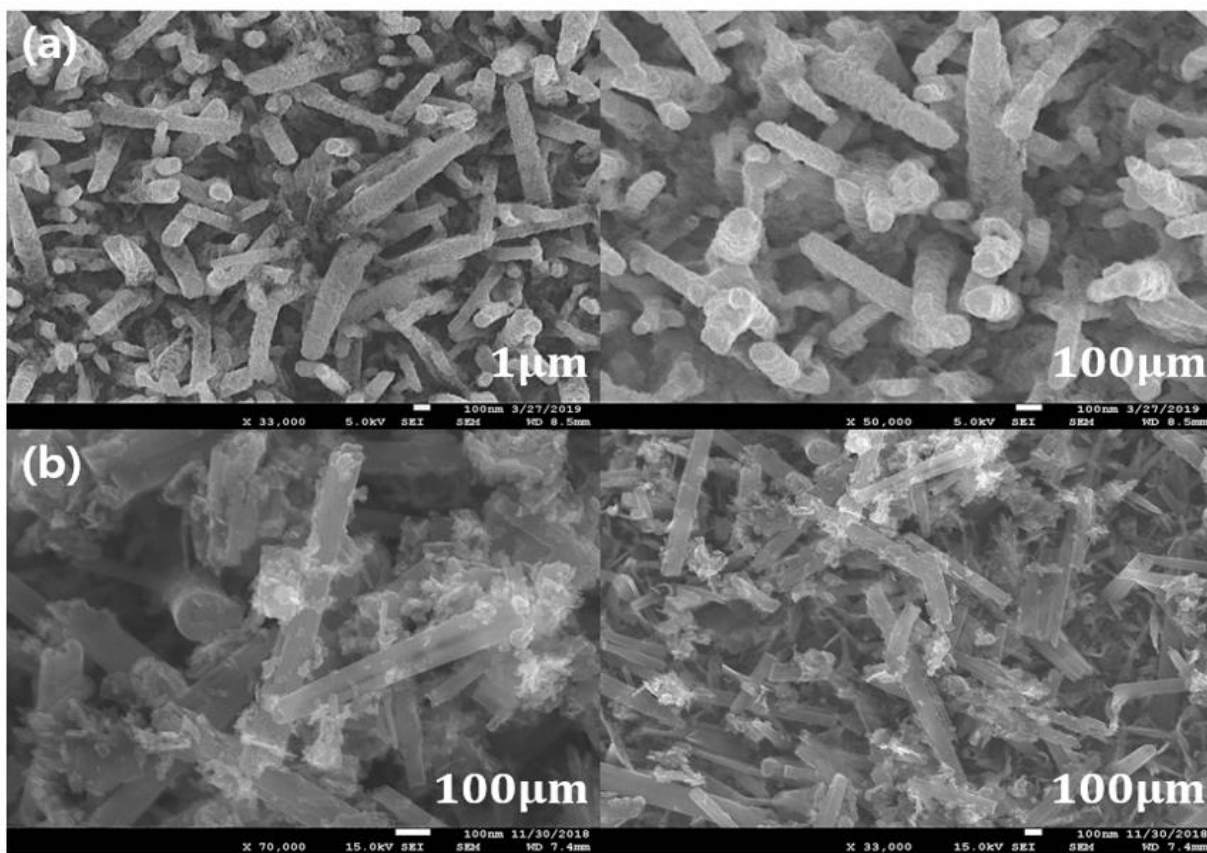
Figure 8. Porous Ti nanorods on a metallic Ti substrate (a) after HCl etching and (b) before HCl etching
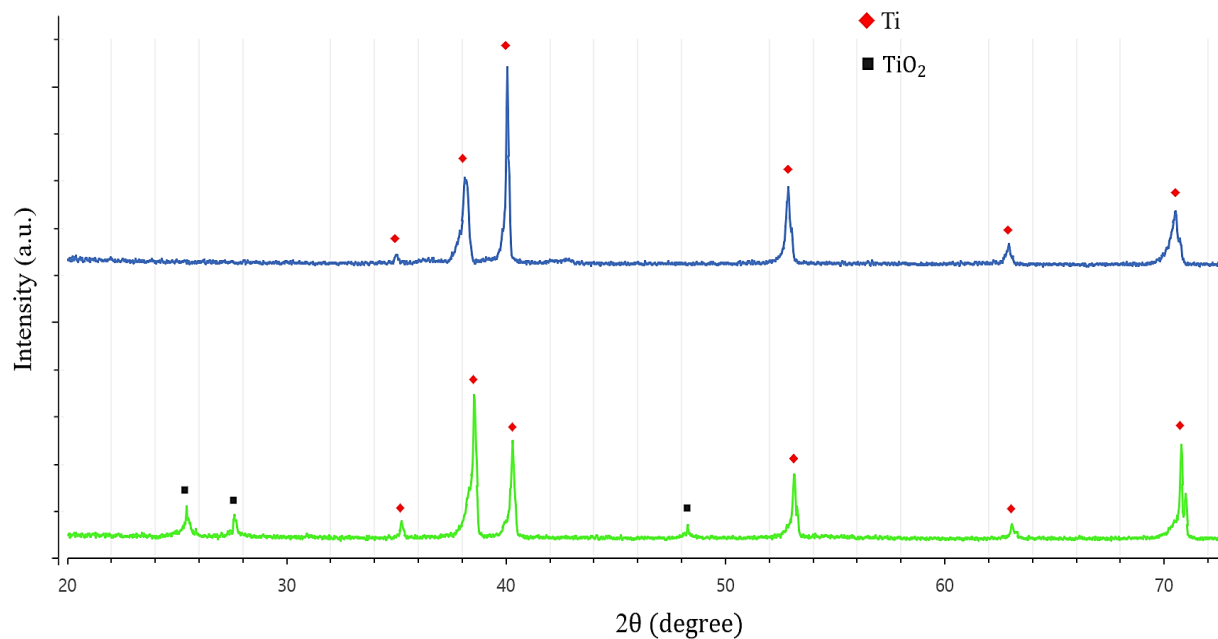
Figure 9. XRD patterns of the Ti nanorods (blue) and the TiO_2 nanorods (green). TiO_2 successfully reduced to Ti via the magnesiothermic reduction.

temperature for 4 hours under the protection of argon flowing rate at a 100 sccm. The set

temperature of 650 °C was wisely selected based on melting points of Mg and Ti. Since the

melting points of Mg and Ti are 650 °C and 1668 °C, respectively, Ti nanorods arrays were still

preserved during the reduction. A possible reaction stoichiometry is shown in Equation 20:

$$2Mg + TiO_2 \rightarrow 2MgO + Ti \tag{20}$$

The sample was then etched by an HCl solution (0.5 M) to remove Mg and MgO and dried in a

vacuum oven to prevent further undesirable reactions. By reducing TiO_2 to metallic Ti, not to

mention the high porosity of the Ti nanorods (Figure 8), a drastic improvement in the electrode

conductivity was achieved [68-69]. The X-ray diffraction (XRD) analysis confirmed that TiO_2

was successfully reduced to Ti (Figure 9). The porous Ti nanorods sample showed a black color,

suggesting the ability of Ti nanorods to absorb nearly all the incident light (Figure 10a). The low

reflectance of the sample was further confirmed by the diffuse reflectance measured by the

JASCO V-570 spectrophotometer in the wavelength range from 200 to 2,000 nm (Figure 10b).

As shown in the spectral reflectance measurement (Figure 10b), reflectivity of the black Ti

sample is substantially low: less than 4% of most visible light and less than 5% of most infra-red

lights. This is because of the multi-directional and porous nature of the Ti nanorods. The

amplitude of forced vibration decreases as light is transmitted and absorbed due to high porosity

of the nanorods (Figure 10c). The outstanding ability to absorb light can be also potentially used

for the applications in which the heat localization is required, such as the solar energy harvesting

and thermoplasmonics [70]. The porous Ti nanorods sample was then finally incorporated into a

2032 coin cell with a polished Li metal foil, 1 M solution of $LiPF_6$ in a 50:50 (v/v) mixture of EC

and DEC, and polypropylene/polyethylene/polypropylene (PP/PE/PP) tri-layer membranes
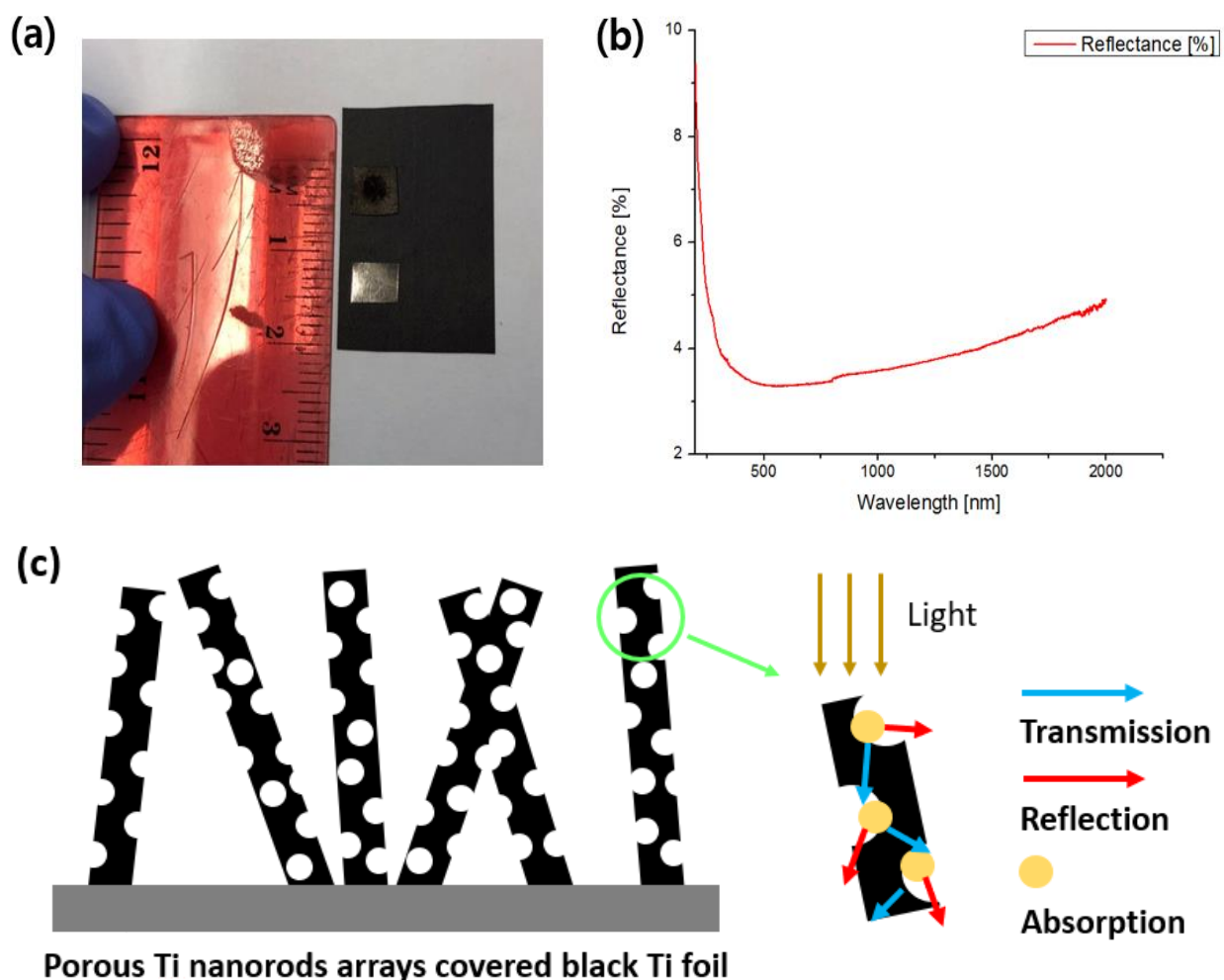
Figure 10. (a) Comparison of colors between the Ti nanorods and the pure Ti samples. While the pure Ti sample exhibits a shiny metal color, the Ti nanorods exhibits a block color. (b) Diffuse reflectance measurement of the Ti nanorods sample with the wavelength range from 200 to 2,000 nm. (c) Schematic illustration of the behavior of incoming light on the metallic Ti nanorods.

(Celgard 2320) as a counter electrode, an electrolyte, and a separator, respectively. For control experiments, a planar metallic Ti substrate was incorporated in a cell as a working electrode instead of the Ti nanorods sample. The cell assembly was carried out in an argon-filled glovebox. In the following section, the morphological evolution of the Ti nanorods as a function of Li

electrodeposition time is proposed.

4.3) Morphology Study

The analysis of the morphological changes as a function of the lithiation time proceeded by the field emission scanning electron microscopy (FESEM; JEOL 7600 coupled with energy-dispersive X-ray spectroscopy, EDX), with the accelerating voltage of 15 kV before the galvanostatic cycling of coin cells. Li plating was performed at a current density of 1 mAh/cm^2. As discussed, it has been confirmed that Gibbs transformation energy of a nucleus becomes low at the heterogeneous nucleation sites [51-55]. As Abyaneh [51] descried electrochemical heterogeneous nucleation models as a conical-shaped cavity, similarly, given the highly porous nature, the Ti nanorods provide such preferential nucleation sites for Li. At the initial stage of the lithiation, it is clearly shown that Li tends to deposit on the surface of the Ti nanorods rather than a flat Ti substrate due to substantial surface area provided by the Ti nanorods (Figure 11a). It is noteworthy that multi-directional nanorods arrays engage the lateral Li electrodeposition on the nanorods. Therefore, after the initial Li electro-crystallization on the nanorods, local Li ion flux is accelerated on the bodies of the nanorods due to low energy barrier, leading to the morphology change I refer to 'fat nanorods' (Figure 11b). Continuous lateral Li growth on the bodies of the nanorods results in the physical contact between adjacent nanorods, resulting in the coalescence of nanorods (Figure 11c). As a result, as Li plating proceeds, the Ti nanorods become fully covered by Li without Li dendrites (Figure 11d-11e). Figure 11f shows the top image of the Ti nanorods after 24 hours of Li electrodeposition. A smooth surface shown in Figure 11f suggests that the undesirable Li dendrite formation was completely avoided even after 24 hours of Li plating, implying that the stabilization of the SEI layer and homogeneously distributed electric

27
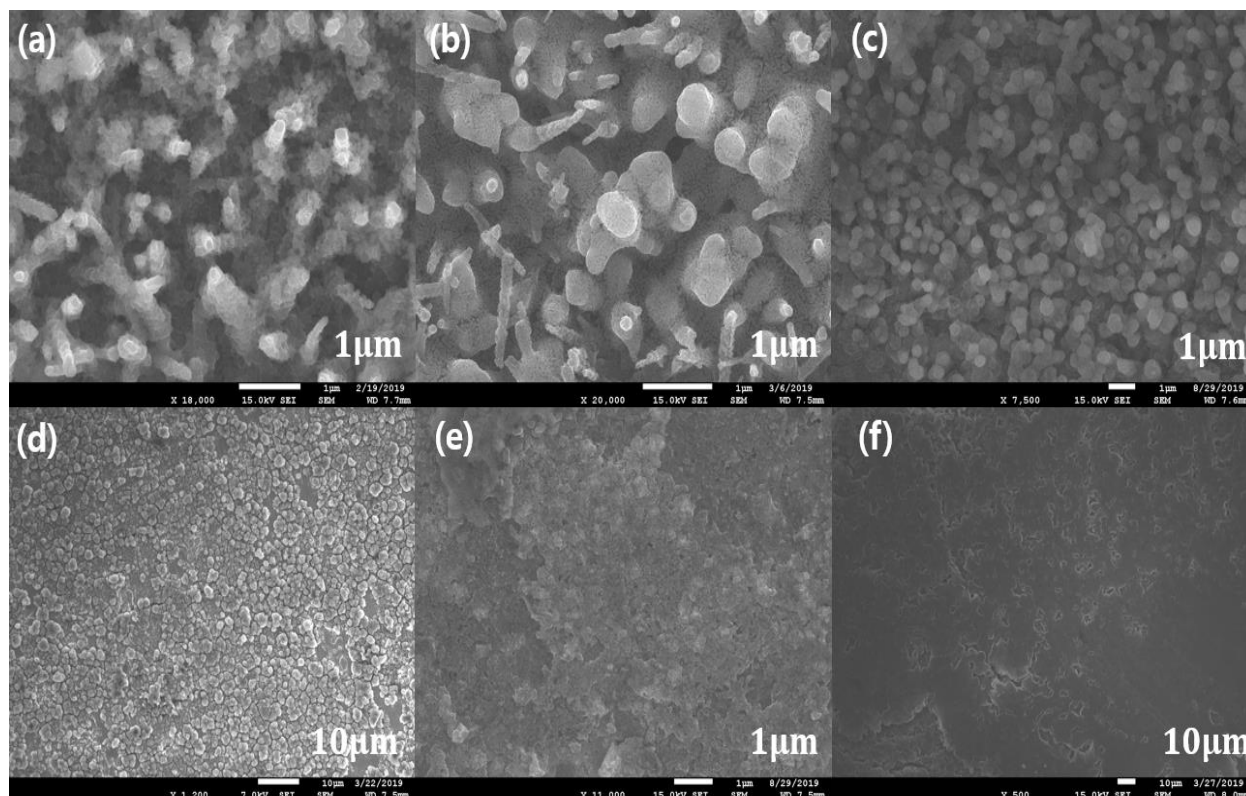
Figure 11. Morphological changes of the Ti nanorods as a function of Li plating time, starting from (a). (a) Li deposits on the porous Ti nanorods due to high surface area, (b) Li laterally grows on the bodies of the nanorods, resulting in the formation of 'fat nanorods', and (c)~(e) continuous Li plating results in the complete immersion of Ti nanorods with no Li dendrite formation. As a result, (f) even after 24 hours of Li plating, Li dendritic growth was successfully avoided.
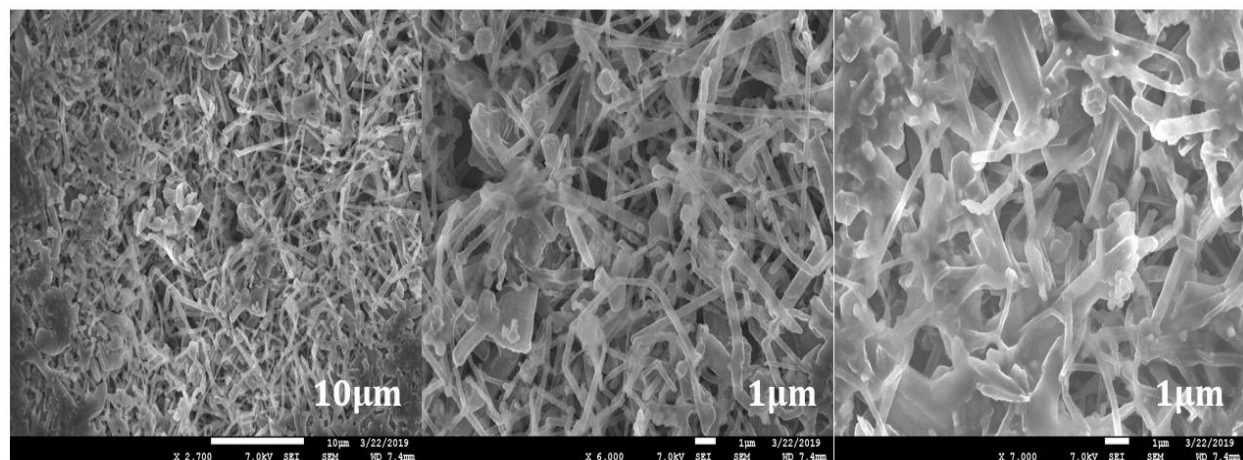
Figure 12. Top images of a pure Ti substrate after 24 hours of Li deposition. Dendrite formation found.
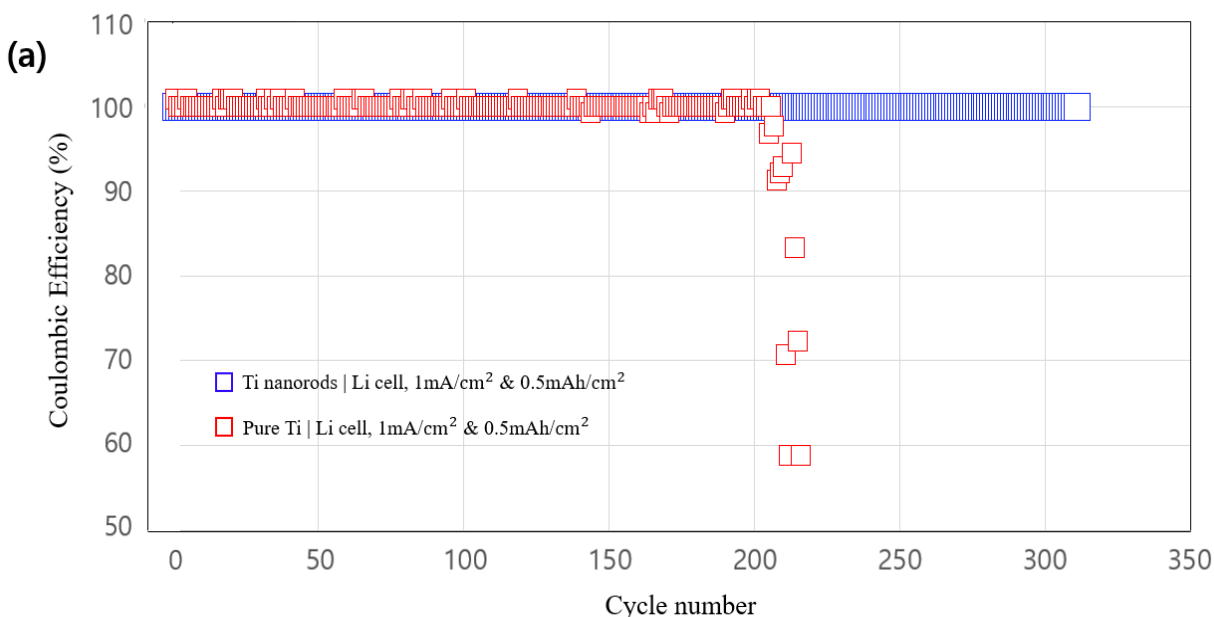
Figure 13. The Coulombic efficiency of Li stripping/plating after 24 hours of Li plating. The red square indicates the pure Ti | Li coin cell, while the blue square indicates the Ti nanorods | Li cell.

field were achieved. In contrast, due to the unstable SEI layer and infinite volume changes of the Li metal, sharp Li dendrites were observed on a flat Ti substrate after 24 hours of Li electrodeposition (Figure 12).

4.4) Results & Discussion

It should be noted that before evaluating the electrochemical performance of the cells, the lithiation of both Ti nanorods and pure Ti samples were electrochemically preceded. The lithiation, as discussed in the section 4.3, was simply achieved by discharging Li on both Ti samples on the MTI BST8-WA battery tester. The lithiation proceeded for 24 hours at a current density of 1 mAh/cm^2. After the lithiation process, both Ti nanorods | Li and pure Ti | Li cells were galvanostatically discharged and charged at a current density of 1 mAh/cm^2 and a capacity of 0.5 mAh/cm^2 under ambient conditions. As shown in Figure 13, the Coulombic efficiency of

Li stripping and plating of the pure Ti | Li cell, which describes the reversibility of the cell by the ratio of the amount of Li stripping to Li plating, substantially decreased below 60 % in less than 200 cycles. It must be noted that unlike the Coulombic efficiency presented in many science articles, which is typically obtained by specifying a charge/discharge voltage range and current density, the Coulombic efficiency obtained in this experiment is not a capacity-based parameter: it is simply obtained from the raw data of the galvanostatic cycling test. In other words, since the capacity and current density were fixed in the test, the Coulombic efficiency, which is simply the amount of Li participated in charge/discharge processes, should remain 100 % throughout the whole cycle for both coin cells. However, the electrical disconnection caused by Li dendrites, accumulated dead Li on the anode, and high interfacial impedance hampered the free ionic flux during charging, resulting in poor reversibility. In contrast, the Ti nanorods | Li cell exhibited an exceptional improvement in reversibility with 100 % of the Coulombic efficiency more than 1,400 cycles, indicating that the stable SEI layer and the uniform Li electrodeposition were achieved with no dendrites. The exceptional electrochemical performance of the Ti nanorods | Li cell was further proved by a long-term galvanostatic cycling behavior (Figure 14). The voltage polarization of Li plating/stripping of the Ti nanorods | Li cell was maintained at ~8 mV for than 1,400 cycles as shown in Figure 15. Although voltage fluctuation was observed at the 97 cycle, discharge and charge voltages were -30 mV and 35 mV, respectively, which are negligibly small. This temporal voltage fluctuation could be attributed to an external disturbance that occurred in a laboratory. On the other hand, the pure Ti | Li coin cell showed a significantly high voltage hysteresis throughout the whole testing (Figure 14a). The stripping/plating overpotential of the pure Ti | Li coin cell was reached to 120 mV in 100 cycles and rapidly diverged, reaching to 300 mV in 200 cycles (Figure 14a). Such considerably large voltage polarizations imply an
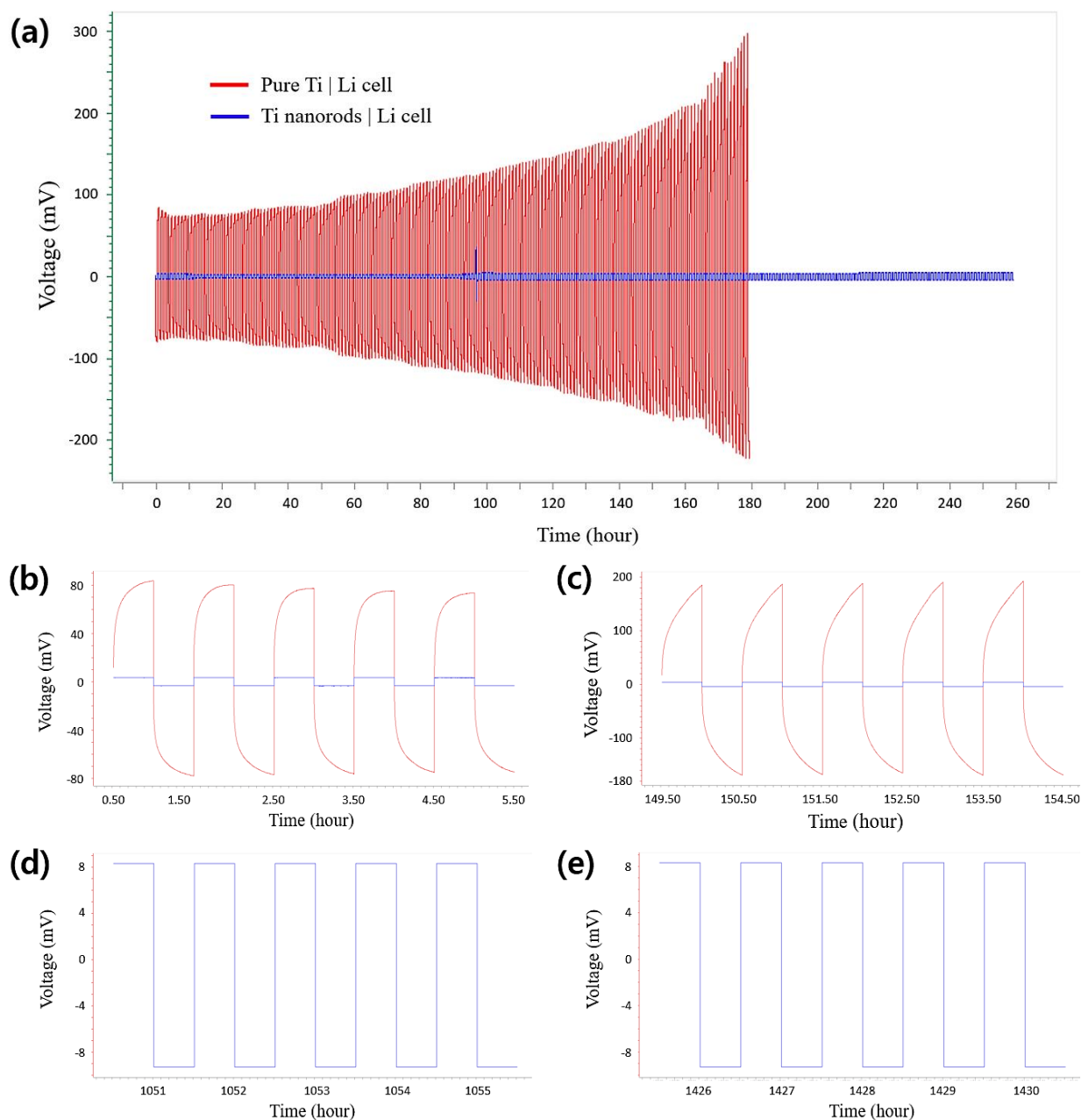
Figure 14. Galvanostatic discharge/charge voltage profiles. The red line indicates the pure Ti | Li coin cell, while the blue line indicates the Ti nanorods | Li cell. The voltage hysteresis of the Ti nanorods | Li cell was maintained at ~8 mV for more than 1,400 hours.

an increased interfacial resistance as well as capacity decay caused by Li dendrites. The entire discharge/charge voltage profiles of both pure Ti | Li and Ti nanorods | Li coin cells after 24
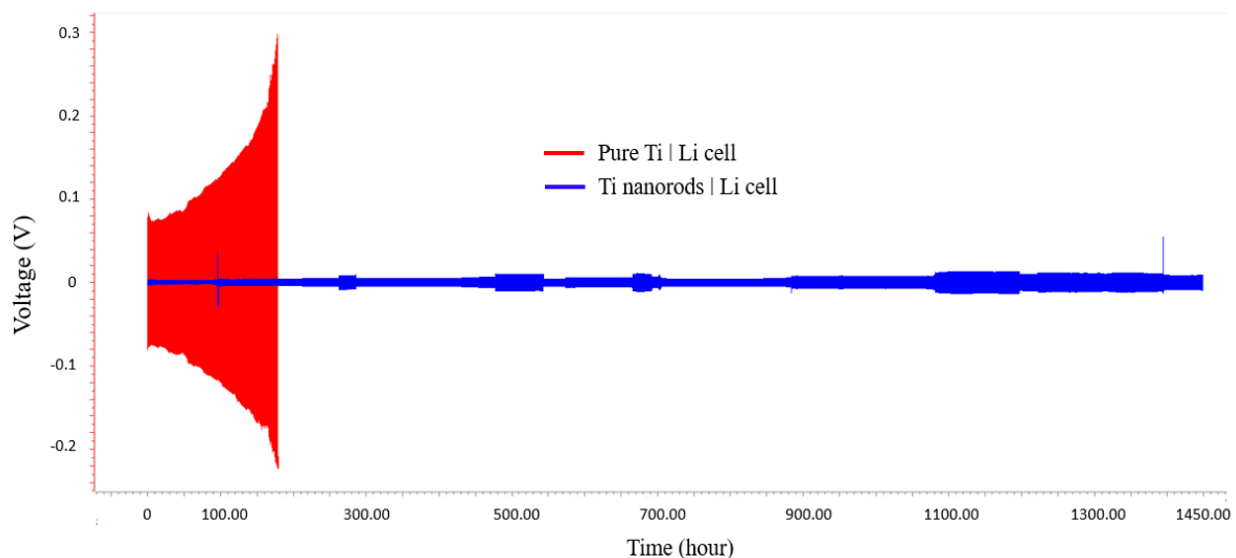
Figure 15. Galvanostatic discharge/charge voltage profiles after 24 hours of Li electrodeposition. The red line indicates the pure Ti | Li coin cell, while the blue line indicates the Ti nanorods | Li cell. The voltage hysteresis of the Ti nanorods | Li cell was maintained at ~8 mV for more than 1,400 hours.

hours of Li electrodeposition is shown in Figure 15. To investigate the effect of lithiation time on the functionality of the Ti nanorods, long-term galvanostatic cycling behaviors of the Ti nanorods | Li coin cells after 12, 18, and 24 hours of lithiation are obtained (Figure 16a). The coin cell after 12 hours of lithiation exhibited the largest voltage hysteresis with an initial discharge and charge voltage of ~60 mV. Overall, the coin cell after 18 hours of lithiation showed a relatively smaller voltage polarization compared to that after 12 hours of lithiation. However, after 180 cycles, the charge/discharge overpotential started diverging rapidly, and the discharge overpotential of the coin cell after 18 hours lithiation became greater than that after 12 hours of lithiation. This could be attributed to poor conditions of a sample, such as the low density of Ti nanorods throughout the substrate due to the excessive amount of Mg powder used in the magesiothermic reduction or a damage obtained while assembling the coin cell. The coin cell after 24 hours of lithiation, as expected, showed the narrowest voltage hysteresis throughout
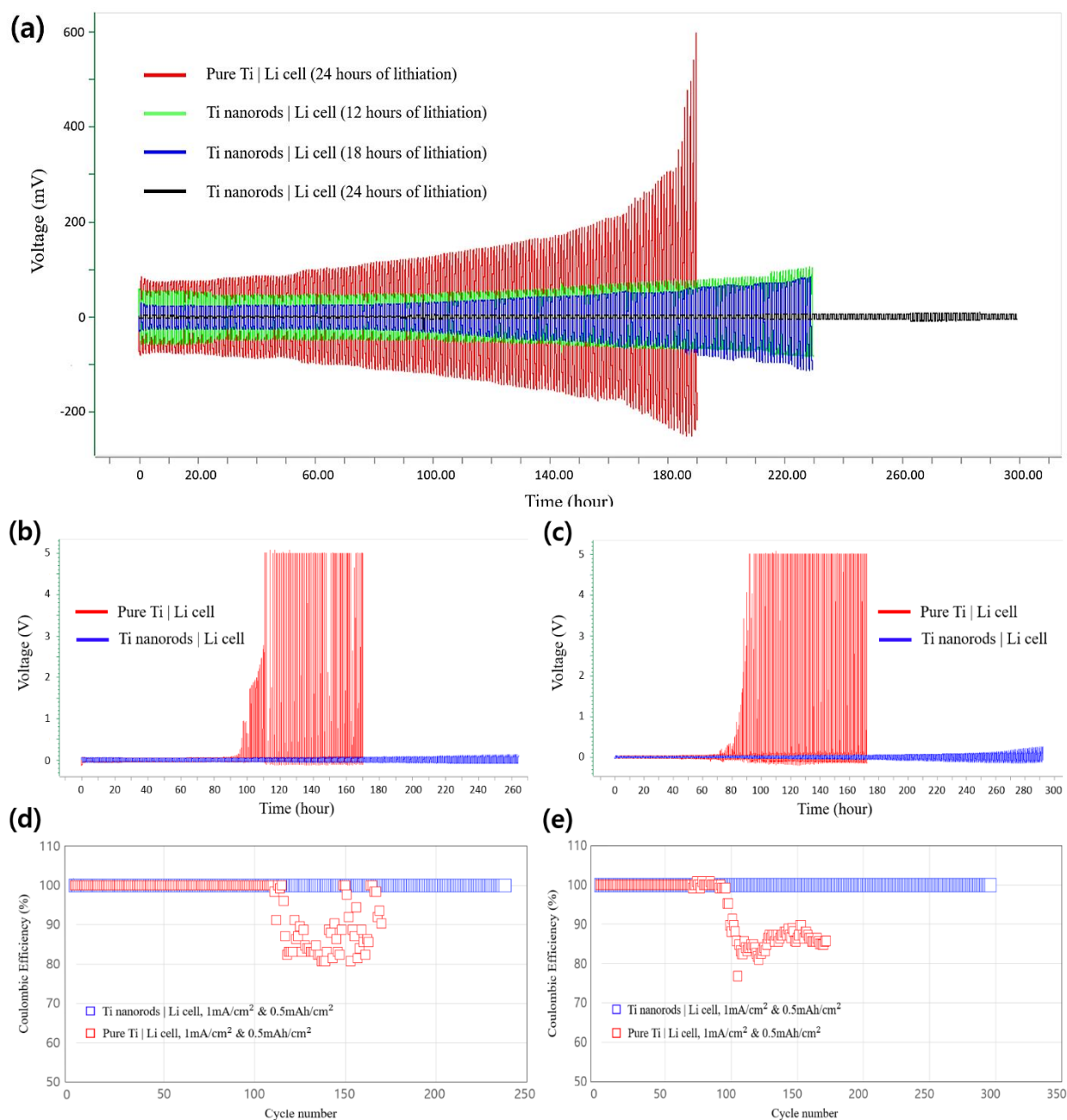
Figure 16. The electrochemical cycling performance of Ti nanorods | Li and pure Ti | Li coin cells. (a) Galvanostatic discharge/charge voltage profiles of the pure Ti | Li cell (red) and the Ti nanorods | Li cells after 12 (green), 18 (blue) and 24 (black) hours of Li electrodeposition. Galvanostatic discharge/charge voltage profile after (b) 12 hours and (c) 18 hours of lithiation, and the Coulombic efficiency after (d) 12 hours and (e) 18 hours of lithiation.

the whole cycle, which leads to a conclusion that the lithiation time contributes to the stability of the Ti nanorods | Li coin cell. This behavior is theoretically explainable: as Li continuously deposits on the Ti nanorods, the electrochemical potential difference between the Li metal and the lithiated Ti nanorods becomes smaller, lowering the energy cost. More importantly, it should be noted that regardless of the amount of lithiation time, the Ti nanorods significantly contributed to the enhancement in the electrochemical performance. To prove this point, the electrochemical stability of the Ti nanorods | Li coin cells after 12 and 18 hours of lithiation were compared to that of the pure Ti | Li cells after 12 and 18 hours of lithiation as shown in Figure 16b and 16c, respectively. Both pure Ti | Li cells after 12 and 18 hours of lithiation exhibited unstable voltage profiles, rapidly fluctuating after 80 cycles. On the other hand, the Ti nanorods | Li cells exhibited a substantial improvement in the stability. The improved electrochemical performance of the Ti nanorods | Li cells after 12 and 18 hours of lithiation was further confirmed by the outstanding Coulombic efficiency that remained 100 % throughout the whole cycle as shown in Figure 16d and 16e, respectively. The superior functionality of the multi-directional Ti nanorods to guide the uniform Li electrodeposition was demonstrated. The pre-lithiated Ti nanorods before the cycling provides potential applications of fully charged-state batteries as a stably lithiated anode material when incorporated with a Li-free cathode. Potential candidates for a Li-free cathode material include transition metal oxyfluorides, such as VO_2F and BiOF [71].

CHAPTER 5. BMS: LITHIUM-ION BATTERY MANAGEMENT SYSTEM

To fully take advantage of the high power, energy density and cyclability of Li-ion batteries, attempts to use Li-ion batteries for automobile applications, such as electric vehicles (EVs) and hybrid electric vehicles (HEVs), have been intensely made. Since the electrochemistry of Li-ion batteries is very sensitive, abusive battery operations negatively affect the performance of Li-ion batteries. For example, during over-discharging, the decomposition of the SEI layer caused by the over-deintercalation of Li-ions engages the formation of new SEI layers on the anode during the following charging process, increasing the interfacial impedance. Moreover, undesirable side reactions caused by an abnormal increase in the anode potential lead to capacity degradation [72]. The consequences of the over-discharging of a battery cell are not ignorable as it can eventually induce the internal short circuit and thermal runaway. Such an abusive battery operation often occurs in a battery module and pack because it is highly challenging to keep track of parameters that are crucial to the operation of Li-ion batteries due to the highly complex nature of the large-scale battery system. For this reason, continuous monitoring of critical parameters of each battery cell, such as voltage and temperature, and accurate estimations of the state of charge (SOC) and the state of health (SOH) are imperative. This can be achieved by a proper battery management system (BMS). A successful BMS can maximize the electrochemical performance and the cycle life of battery cells under various operating conditions. Main functions of a BMS are as follows:

1) Monitoring voltage, current and temperature of a cell

2) Estimation of the SOC and the SOH

3) Cell balancing

4) Isolation of the battery pack

5) Control of the battery charging profile and parameters, such as input and output power

Typically, measured voltages of individual cells are used to estimate the SOC. However, the cell voltage is not sophisticated enough to capture the highly non-linear dynamics of the battery aging mechanism. Although intensive research work to obtain a better estimability of the SOC by modeling and studying Li-ion battery behaviors has been reported [73-76], since the complexity of a BMS can increase the cost when building it physically or computational efforts when simulating, challenges remain. Measured current profiles are generally used to obtain the internal resistance of each battery cell. The internal resistance is a critical parameter since it governs the rapid initial voltage drop during discharging. Temperature is also a necessary parameter to measure and control since it can affect the SOH as well as the SOC. Moreover, an imbalance in temperature between battery cells cause severe safety concerns. The effect of the operating temperature on the performance of a battery cell is specifically discussed in Chapter 6. Since a direct SOC measurement method is currently non-existent, the SOC can be only estimated. Although traditional methods to estimate the SOC, such as the open circuit voltage (OCV) method and the Coulomb counting method, show moderate accuracy in some cases, these traditional approaches are not based on the Li-ion battery chemistries that have a highly non-linear OCV-SOC behavior. Thus, a battery model-based SOC estimation method becomes a popular strategy. Existing battery models that can capture the Li-ion battery chemistries can be classified into three major categories:

1) Mathematical models
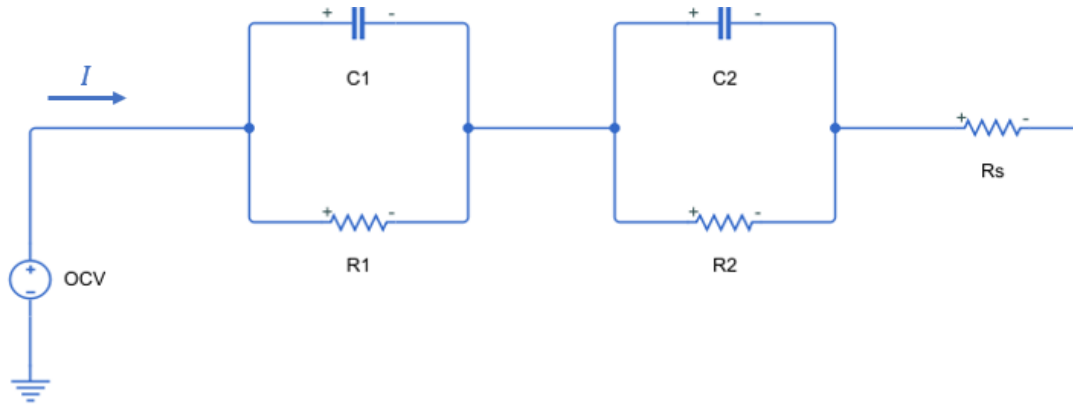
Figure 17. A general equivalent circuit model.

2) Electrochemical models

3) Equivalent circuit models (ECMs)

The mathematical models predict the battery runtime, efficiency, and capacity by using empirical relations. However, most of the mathematical models provide inaccurate results, and these models are only applicable to limited applications. The electrochemical models are developed based on the underlying physics of electrochemical reactions occurred in a battery cell. Even though these models are highly accurate, such highly complicated models require significant computational efforts. In system-level simulations, such as BMSs for EVs or HEVs, ECMs are considered to be the most suitable model due to its high accuracy and reasonable computation efforts [77]. In ECMs, battery components are represented by a voltage source, resistors and capacitors, which collectively reflect the open circuit potential, the internal resistance, and the relaxation time of a Li-ion battery cell to capture the electrochemical behaviors. The typical ECM is depicted in Figure 17. The voltage circuit included is associated with the open circuit potential. The R_s, which is related to the ionic conductivity of the separator and the electrolyte, is the internal resistance that causes the rapid terminal voltage drop once a

load is connected. The resistor-capacitor (RC) branches, which capture the intercalation and deintercalation dynamics of Li ions, account for the time constants and the frequency response of the battery. These elements of an ECM are typically dependent on the operating temperature and the SOC. For the parameterization of the equivalent circuit elements, two methods are traditionally used. The first method uses the Thévenin theorem to measure the voltage of a battery cell generated by a DC pulse. Because of the temperature and SOC dependencies of the equivalent circuit elements, the DC pulses must be applied at different SOC and temperature values for an accurate parameterization. However, this method is not capable of a full parameterization of the equivalent circuit elements. Moreover, this method cannot capture the underlying physics inside a battery cell, such as the charge transfer and the diffusion. Alternatively, the electrochemical impedance spectroscopy (EIS) method has gained much attention for the parameterization of Li-ion batteries. One of the advantages of this method is that it is generally non-destructive to the investigated electrochemical system, which allows for further measurements and investigations. Typically, an alternative current (AC) response caused by an applied sinusoidal AC potential with varying frequencies is measured. Using a Fourier series, the AC response can be analyzed as a sum of sinusoidal functions, further allowing for the calculation of the impedance, often denoted as Z. The calculated impedance is generally represented by the Nyquist and the Bode plots. The EIS method can capture the underlying physics of a battery cell. Furthermore, a full parameterization is possible with this method. However, the EIS measurements also suffer from its own disadvantage: it can be only performed at low C-rates since the SOC of a Li-ion battery cell can be changed during the highly time-consuming EIS measurements [77]. For this reason, developing new parameterization methods has become one of the most in-demands research areas. As for the estimation of the SOH, since

degradation of Li-ion batteries causes capacity decay and an increase in the internal resistance, complete full charge and discharge profiles for each cell are required. The updated profiles are used for calculations of the capacity lost. The SOH can be estimated by Equation 21:

$$\text{SOH } [\%] = \frac{C_m}{C_{rated}} * 100 \qquad (21)$$

where C_m [Ah] is the maximum capacity and C_{rated} [Ah] is the rated capacity. Cell balancing is very important in a BMS since an imbalance in critical parameters, such as temperature and SOC, can lead to abusive battery operations, causing severe capacity deterioration and more importantly, safety issues. The balancing approaches can be classified into two categories: passive and active balancing. The passive balancing approach extracts extra charges from overcharged cells and remove them through an external resistor until the charge balance is achieved. In contrast, the active balancing approach distributes the extra energy to other cells. Isolation of the battery pack is typically achieved by shutting down the current when values of certain parameters, such as temperature and voltage, go beyond their limits. For all these BMS tasks, the controllability of the battery discharging/charging profiles and parameters is necessary. Many software programs commercially available provide the capability to develop a BMS. Among them, the MATLAB/Simulink provides exceptional modeling and simulation capabilities that allow for the development of a proper BMS. Using the MATLAB/Simulink, an online estimation of the SOC and the SOH, a validation of a BMS model by real-time simulations, and a parameterization of the ECM elements can be efficiently achieved. As discussed, developing a proper BMS is necessary for the safe and efficient operation of Li-ion batteries. Besides the main functions of a BMS, maintaining the optimal operating temperature of Li-ion batteries is also

imperative due to the poor heat tolerance of Li-ion batteries. For this reason, in Chapter 6, a Li-ion battery thermal management system is discussed.

CHAPTER 6. BTMS: LITHIUM-ION BATTERY THERMAL MANAGEMENT SYSTEM

6.1) Introduction

A battery thermal management system is a must technology for large-scale Li-ion battery applications, such as EVs and HEVs. Since a single Li-ion battery cell provides low power and voltage, Li-ion battery modules and packs in which Li-ion battery cells are connected in series and parallel are used to meet the high-power requirements of these applications. The heat generated from electrochemical reactions and resistances in a Li-ion battery cell during charging and discharging must be appropriately dissipated as the operating temperature has significant impacts on the battery cell:

1) Cycle life

2) Safety

3) Power and energy capability

4) Functionality of the electrochemical system

The optimal operating temperate range for Li-ion batteries is between 15 °C and 35 °C [78], and the maximum temperature difference between cells and modules should be within 5 °C. The low temperature operation can cause an increase in the internal resistance and decelerate the free ionic flux, which can eventually lead to a decrease in a unit cell voltage. The high-temperature operation raises safety concerns, which can eventually lead to thermal runaway and cell explosion. Moreover, the non-uniform distribution of temperature in a battery cell, module, and pack can accelerate the aging mechanism and capacity deterioration. To maximize the electrochemical performance of Li-ion batteries, the optimal temperature operation as well as the

uniform temperature distribution throughout the battery system must be achieved by the implementation of a proper battery thermal management system (BTMS). BTMSs can be mainly classified into three types: passive cooling systems [79-80], active cooling systems [81-84], and hybrid active-passive cooling systems [85]. The passive cooling systems use latent heat of phase change materials (PCMs) to decrease the operating temperature. In contrast, the active cooling systems simply use sensible heat of fluids, such as air and water, to cool down the operating temperature. The hybrid cooling systems, as expected, use both latent and sensible heat of cooling medium. A tremendous amount of theoretical and experimental research on Li-ion BTMSs has been previously reported [79-85]. Although experimental research work may provide a great insight into the development of BTMSs, numerical investigations are attracting much attention due to its cost effectiveness and visualization effect. Many commercial software products, such as ANSYS Fluent, COMSOL Multiphysics, and MATLAB/Simulink, provide useful and versatile simulation tools to model a BTMS. Among them, the ANSYS Fluent has become one of the most popular computational fluid dynamics (CFD) simulation tools owing to its broad physical modeling capabilities and outstanding ability for the visualization. Among various physical models provided by the ANSYS Fluent, the multi-scale multi-domain (MSMD) battery model is suitable for the CFD analysis of Li-ion batteries due to its capability to handle multi-physics in different solution domains. In the MSMD model, various electrochemical sub-models are also provided:

1) Newman, Tiedemann, Gu, and Kim (NTGK) model

2) ECM

3) Newman Pseudo-two-dimensional (P2D) model

4) User defined E-model

The NTGK model, a semi-empirical electrochemical model, has been intensively used for the 3D thermal modeling of Li-ion batteries because of its simplicity and high accuracy. In the NTGK model, the volumetric current transfer rate is assumed to be a function of the potential difference between two electrodes. Two parameters, *U* and *Y*, are calculated based on an empirical function that has a polynomial form with a specified depth of discharge (DOD) value as a variable. To be specific, the polarization curves are generated based on experimental results, and *U* and *Y* are obtained by performing curve-fitting on the experimental data [86]. The ECM model, as discussed in Chapter 5, uses an electric circuit form to describe the electrochemical dynamic response of Li-ion batteries. In the ECM, the open circuit voltage, resistances, and capacitances are functions of the SOC. Since these functions are expressed by a high order polynomial form, relatively high computational efforts are required. The Newman P2D model is a physics-based model that captures Li-ion transport phenomena and other electrochemical reactions. Although the P2D model exhibits a high level of accuracy, the high complexity of this model induces the difficulty of adjusting parameters to exactly describe modern Li-ion battery chemistries. In the following section, BTMSs for both prismatic and cylindrical Li-ion batteries are presented. The BTMSs were modeled by using the ANSYS Fluent. Since the ANSYS Fluent provides a limited CFD capability for the student license, the 3D thermal analysis of a large cylindrical Li-ion battery pack is not included in this paper; a prismatic Li-ion battery cell and module are only simulated. Instead, a 3D thermal design of a cylindrical Li-ion battery pack is presented. First, a single prismatic Li-ion polymer cell was simulated, and the accuracy of the simulation results was evaluated by using experimental data obtained from Liu et al. [88]. An active cooling system was then incorporated into the cell to efficiently cool down the operating temperature. A BTMS for a prismatic Li-ion battery module in which five Li-ion battery cells are

connected in series was then developed. With the developed battery module, the influences of the inlet velocity and temperature of a coolant were closely monitored. Subsequently, a BTMS for a cylindrical Li-ion battery pack was developed.

6.2) Thermal Modeling of Lithium-ion Batteries (ANSYS Fluent)

The thermal behavior of Li-ion batteries can be analyzed in the ANSYS Fluent. The MSMD battery model and NTGK model are used as a battery model and an electrochemical sub-model, respectively. In the MSMD battery model, battery thermal and electric fields are solved by the following differential equations:

$$\frac{\partial(\rho C_p T)}{\partial t} - \nabla \cdot (k_T \nabla T) = \sigma_+ |\nabla \phi_+|^2 + \sigma_- |\nabla \phi_-|^2 + \dot{q}_{ECh} + \dot{q}_{short} + \dot{q}_{abuse} \tag{22}$$

$$\nabla \cdot (\sigma_+ \nabla \phi_+) = -(j_{ECh} - j_{short}) \tag{23}$$

$$\nabla \cdot (\sigma_- \nabla \phi_-) = j_{ECh} - j_{short} \tag{24}$$

where ρ is the density, C_p is the specific heat capacity, k_T is the thermal conductivity, and T is temperature, respectively. The σ_+ and σ_- are the temperature-dependent electric conductivities, and ϕ_+ and ϕ_- are phase potentials for the positive and negative electrodes, respectively. j_{ECh} and $\dot{q}_{ECh}$ are the volumetric current transfer rate and the heat generated by electrochemical reactions, respectively. The source terms j_{ECh} and $\dot{q}_{ECh}$ are calculated by using an electrochemical sub-model. The j_{short} and $\dot{q}_{short}$, which represent the current transfer rate and the heat generation due to the battery short-circuit, respectively, are equal to zero unless the internal short-circuit is present. The $\dot{q}_{abuse}$, which is normally set to zero, is the heat generated by thermally abusive battery operations. Although the internal short circuit and abusive

operations of Li-ion batteries are not considered in this simulation, more information regarding these source terms can be found [87]. The NTGK electrochemical sub-model then calculates the volumetric transfer current density with the following equation:

$$j_{ECh} = aY[U - (\phi_+ - \phi_-)] \tag{25}$$

where a denotes the specific area of the electrode sandwich sheet, Y and U are the model parameters that are a function of the battery depth of discharge (DOD) expressed by:

$$DOD = \frac{V}{3600Q_{Ah}} \int_0^t j \, dt \tag{26}$$

where V denotes the volume of the battery, and Q_{Ah} is the total electric capacity of the battery in ampere hours, respectively. In this simulation, the voltage-current response curves are obtained through experiments, and Y and U values are obtained by curve fitting the simulation data. The Y and U values are calculated by the following formulations:

$$Y = \sum_5^{n=0} a_n (DOD)^n * e^{-C_1\left(\frac{1}{T} - \frac{1}{T_{ref}}\right)} \tag{27}$$

$$U = \sum_3^{n=0} b_n (DOD)^n * C_2(T_{ref} - T) \tag{28}$$

where C_1 and C_2 are the battery-specific NTGK model constants, and T_{ref} is the reference temperature. The a_n and b_n coefficients are used for calculating Y and U values. Finally, the $\dot{q}_{ECh}$, the heat generated due to electrochemical reactions, is then calculated as:

$$\dot{q}_{ECh} = j_{ECh} * [U - (\phi_+ - \phi_-) - T\frac{dU}{dT}] \tag{29}$$

The first term, $j_{ECh}[U - (\phi_+ - \phi_-)]$, denotes the irreversible heat generated by the overpotential, while the second term, $j_{ECh}T\frac{dU}{dT}$ is the reversible heat generated by entropic heating.

6.3) Prismatic Lithium-ion Battery Cell

The prismatic Li-ion battery cell modeled in this work is the ePLB-C020 Li-ion polymer battery cell with LiNiCoMnO2 as the cathode material. The characteristics of the cell are shown in Table 1.

Quantity	Value
Chemistry	LiNiCoMnO2
Nominal voltage	3.65 V
Cell capacity	20 Ah
Energy density	174 Wh/kg
Power density	2300 W/kg
Height	217 mm
Width	127 mm
Thickness	7 mm

Table 1. Parameters of the cell characteristics and the geometry.

The temperature profile of this cell measured by experiments is provided by Liu et al. [88]. In their experiment, the temperature of nine different locations of a battery cell was measured during full discharging under 25 °C at varying C-rates. A C-rate is a measure of battery charging/discharging rate used to scale the charge/discharge current of a battery cell. For example, a 1C discharge rate describes that the battery will be fully discharged in 1 hour. To be able to compare simulation results with the experimental results, a single Li-ion battery cell was modeled by using the same dimensions shown in Table 1. The modeled battery cell was then
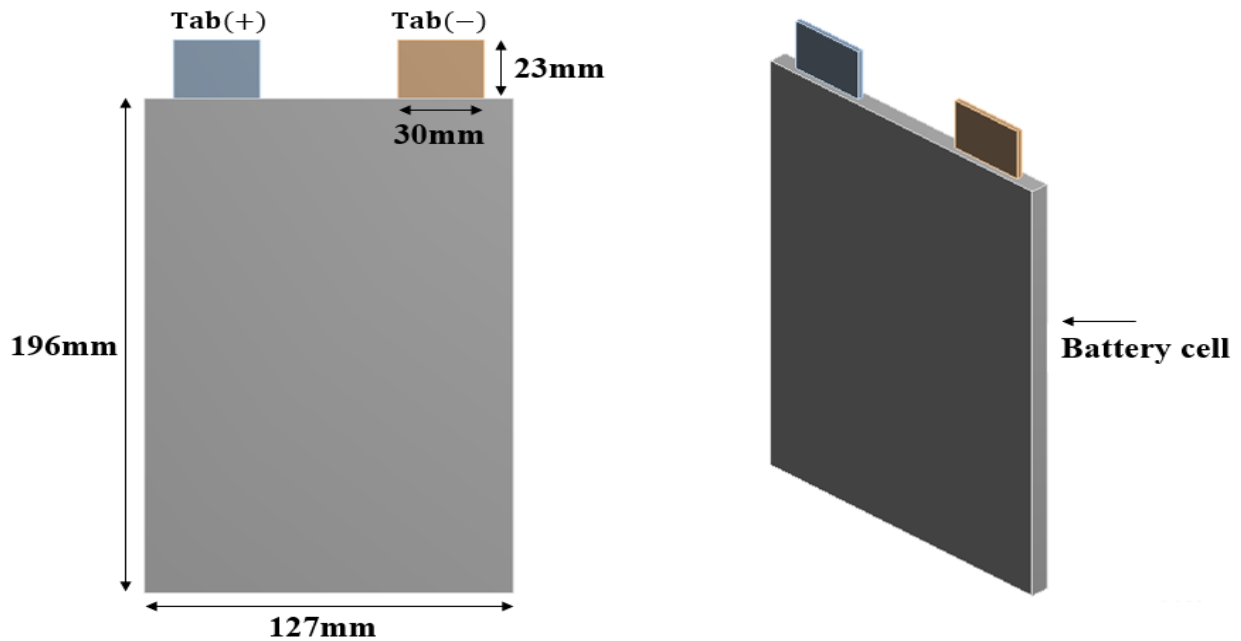
Figure 18. The 3D geometry of the prismatic Li-ion battery cell. The Tab (+) and Tab (-) are positive and negative tabs, respectively.

simulated under the same conditions that the experiments were conducted under. The 3D geometry of the ePLB-C020 Li-ion polymer cell was built in the DesignModeler, which was further imported to the Mesh (Figure 18). Subsequently, in the Mesh, 189,237 nodes and 93,420 elements were generated. The level of the mesh refinement was chosen with consideration of the trade-off relationship between computational efforts and the accuracy of the simulation results. The simulation was conducted based on the experimental setup: the prismatic Li-ion battery cell was set to be fully discharged with the initial DOD value of 0. The operating voltage range was set from 2.5 V to 4.2 V. Copper was assigned for positive and negative tab materials, while the property of active materials in the battery cell was customized to have 2092 kg/m^3, 678 J/kg·K, 18.4 W/m·K, 3.541e+07 siemens/m as the density, specific heat, thermal conductivity, and electrical conductivity, respectively. The User-Defined Scalar Diffusion Coefficients were then
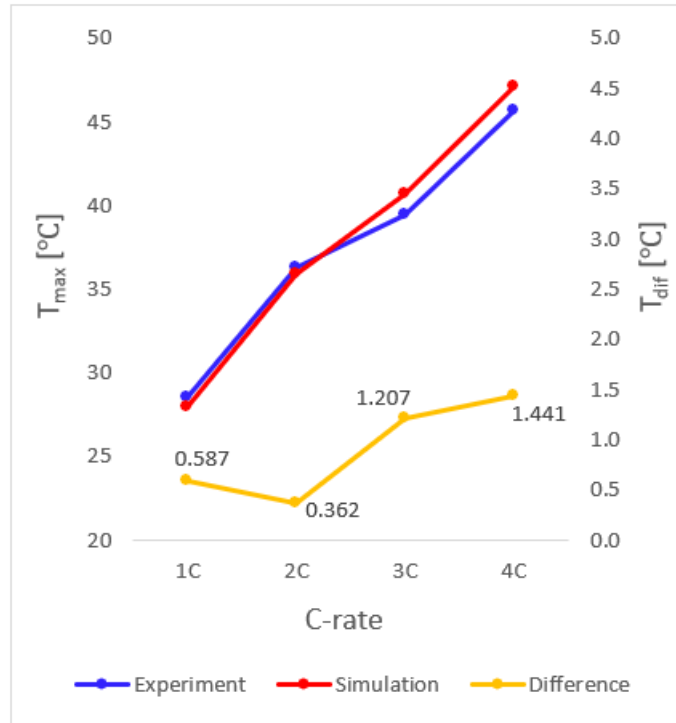
Figure 19. The maximum temperature comparison between experimental (red) and simulation (blue) results. T_{max} is the maximum temperature, and T_{dif} is the maximum temperature difference between the experimental and simulation results.

set to 1,190,000 kg/m·s and 983,000 kg/m·s for uds-0 and uds-1, respectively. For boundary conditions, the heat convection was turned on with 8 W/m^2·K and 298K as the heat transfer coefficient and the free stream temperature, respectively. The boundary conditions of the inlet and the outlet were set as velocity-inlet and pressure-outlet. No slip boundary condition was used for the fluid zones, and a time step of 10.0 s was used for the simulation. First, to validate the simulation model, the transient analysis of Li-ion battery cell was conducted at varying C-rates: 1C, 2C, 3C, and 4C. Experimental results were then compared with simulation results as shown in Figure 19. For the experimental maximum temperature, the highest temperature values measured at each C-rate were selected regardless of their locations. Overall, locations close to
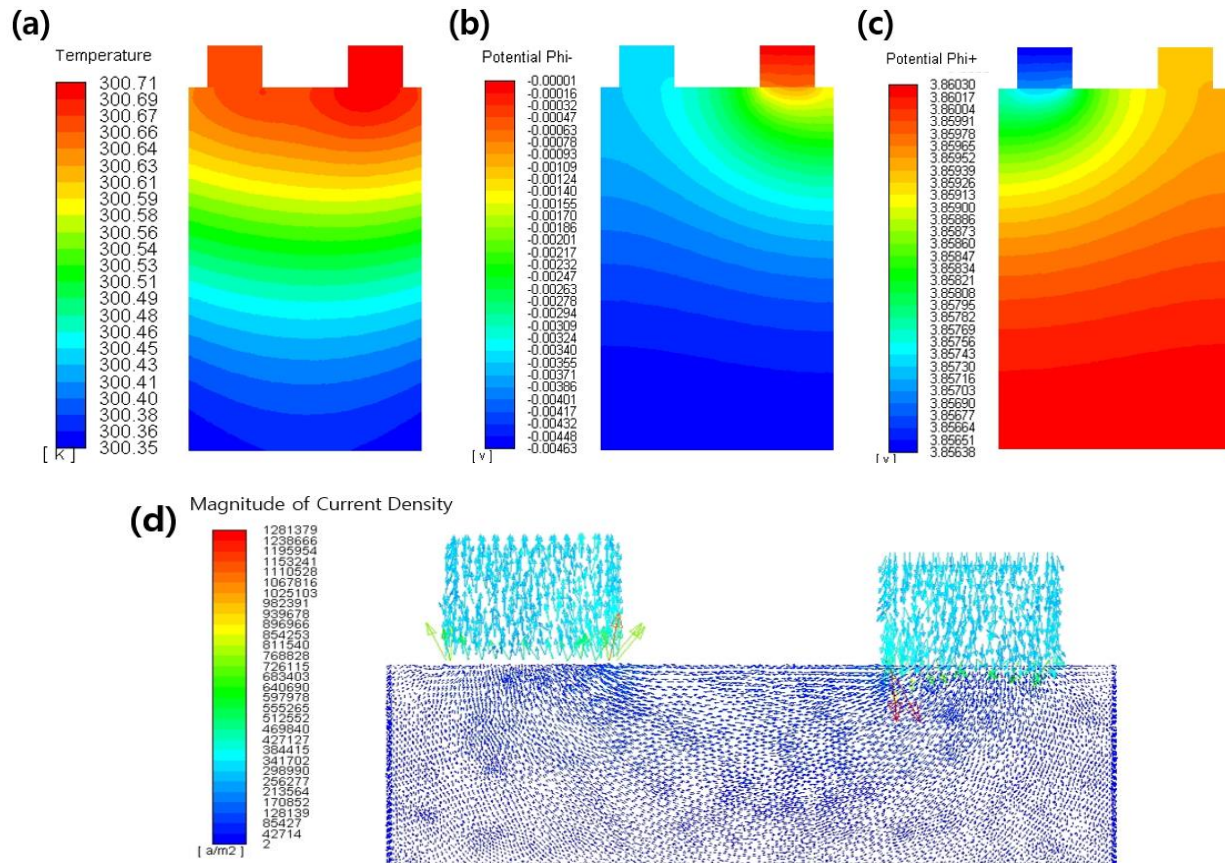
Figure 20. Simulation results of the single prismatic cell at the 1C discharge rate. The contour of (a) temperature, (b) negative potential, (c) positive potential, and (d) vectors of current density.

positive and negative tabs, which connect the current collectors of two electrodes to the external circuits, exhibited higher temperature. As shown in Figure 19, simulation results were in good agreement with experimental results, remaining the maximum temperature difference between the simulation and experimental results less than 1.5 °C throughout the simulations. The simulation results at higher C-rates exhibited relatively high errors from experimental results, which could be attributed to the complex multi-physics nature of the cell. The accuracy of the simulation results can be enhanced by refining the mesh, which is not considered in this paper to avoid the increase in computational efforts. As shown in Figure 19, the operating temperature of
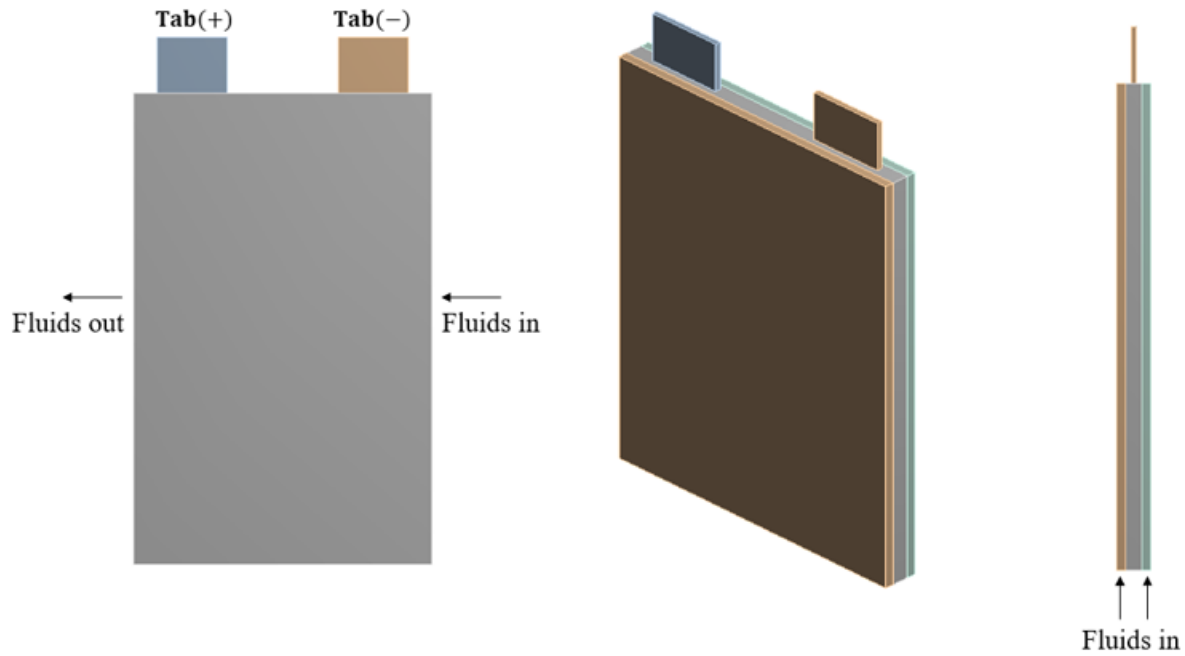
Figure 21. The 3D geometry of the prismatic battery cell sandwiched between cold plates. A coolant flows from the left-hand side to the right-hand side.

battery cells rapidly increases as a C-rate increases, exceeding the recommended maximum operating temperature, which is 35 °C. The temperature contour of the battery cell at the 1C discharge rate is shown in Figure 20a. As confirmed by the experiment, the positive and negative tab areas showed the highest temperature in the cell due to the high current density in the tab areas (Figure 20d). Since the ANSYS Fluent provides outstanding capabilities for the post-processing, contours of other parameters, such as positive and negative potentials, voltage, and electrochemical sources, can be also obtained. For example, the negative and positive potential contours of the battery cell at the 1C discharge rate are shown in Figure 20b and 20c, respectively. The negative and positive potential values were the highest at negative and positive tab areas, respectively. To maximize the electrochemical performance, the single prismatic Li-ion battery cell was sandwiched between cold plates in which coolants flowed from the right-

hand side to the left-hand side with the inlet temperature of 20 °C. The 3D geometry of the battery cell sandwiched between the cold plates is shown in Figure 21. The thickness of the cold plates was 3.5 mm, and copper was used for the cold plate materials. The coolants used in this simulation were the air and water. The inlet velocity of coolants was set to 0.5 m/s. The coolants must satisfy the mass, momentum, and energy conservation equations in the simulation. The governing equations of the coolants are given as follows:

Continuity Equation:

$$\frac{\partial \rho}{\partial t} + \nabla \cdot (\rho \vec{v}) = 0 \tag{30}$$

Momentum Equation:

$$\frac{\partial}{\partial t}(\rho \vec{v}) + \nabla \cdot (\rho \vec{v} \vec{v}) = -\nabla P + \nabla(\tau) + \rho g \tag{31}$$

Energy Equation:

$$\rho C_p \frac{\partial T}{\partial t} + \nabla \cdot (\rho C_p \vec{v} T) = \nabla \cdot (k_T \nabla T) \tag{32}$$

where $\vec{v}$ is the velocity vector, P is the pressure, g is the gravitational acceleration, and τ is the viscous stress tensor. The incorporated cooling system targeted the optimal operating temperature of Li-ion batteries, 15 °C to 35 °C, suggested by [78]. The maximum temperature of the three battery models at varying C-rates is plotted in Figure 22. As a C-rate increases, the operating temperature of the three battery models, the prismatic battery cell with 1) no cooling, 2) air-cooling, and 3) water-cooling, also increased due to the ohmic and entropic heating. The battery cell with no cooling exhibited the highest maximum temperature throughout the whole
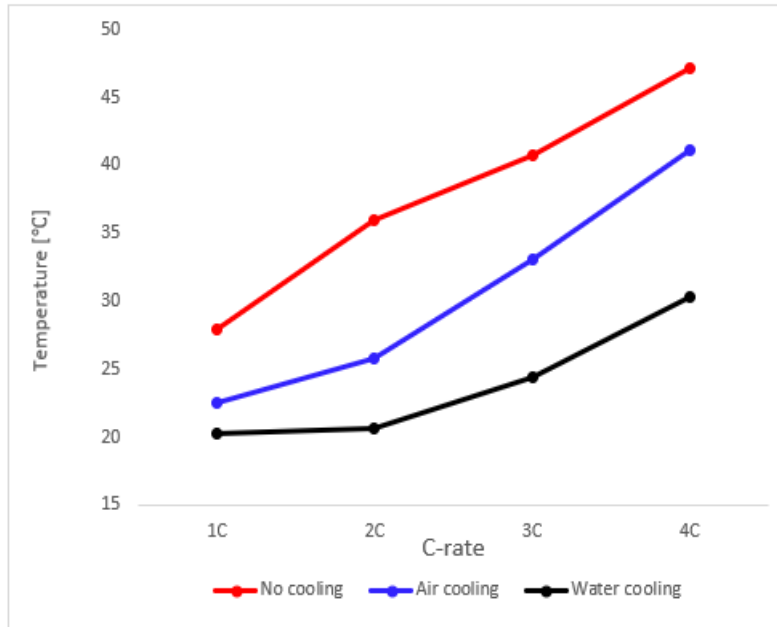
Figure 22. The maximum temperature of the prismatic battery cell with no cooling, air-cooling and water-cooing at varying C-rates: 1C, 2C, 3C, and 4C.

simulations. Although the operating temperature of the battery model with no cooling was in the optimal temperature range at the 1C discharge rate, the temperature of the battery cell significantly increased at the 2C, 3C, and 4C discharge rate, eventually exceeding the maximum optimal temperature of 35 ℃. Such high temperature induced by high C-rates can cause severe safety issues. In contrast, it is clearly shown that the air and the liquid cooling systems effectively dissipated the heat generated in the battery cell. Although the air-cooling battery model successfully remained the maximum operating temperature less than 35 ℃ at the 1C, 2C, and 3C discharge rate, the maximum temperature exceeded 40 ℃ at the 4C discharge rate, which could lead to abusive operations of the battery cell. Overall, the water-cooling battery model exhibited the lowest operating temperature throughout the whole simulations: the maximum operating temperature of the water-cooling battery model successfully remained within the
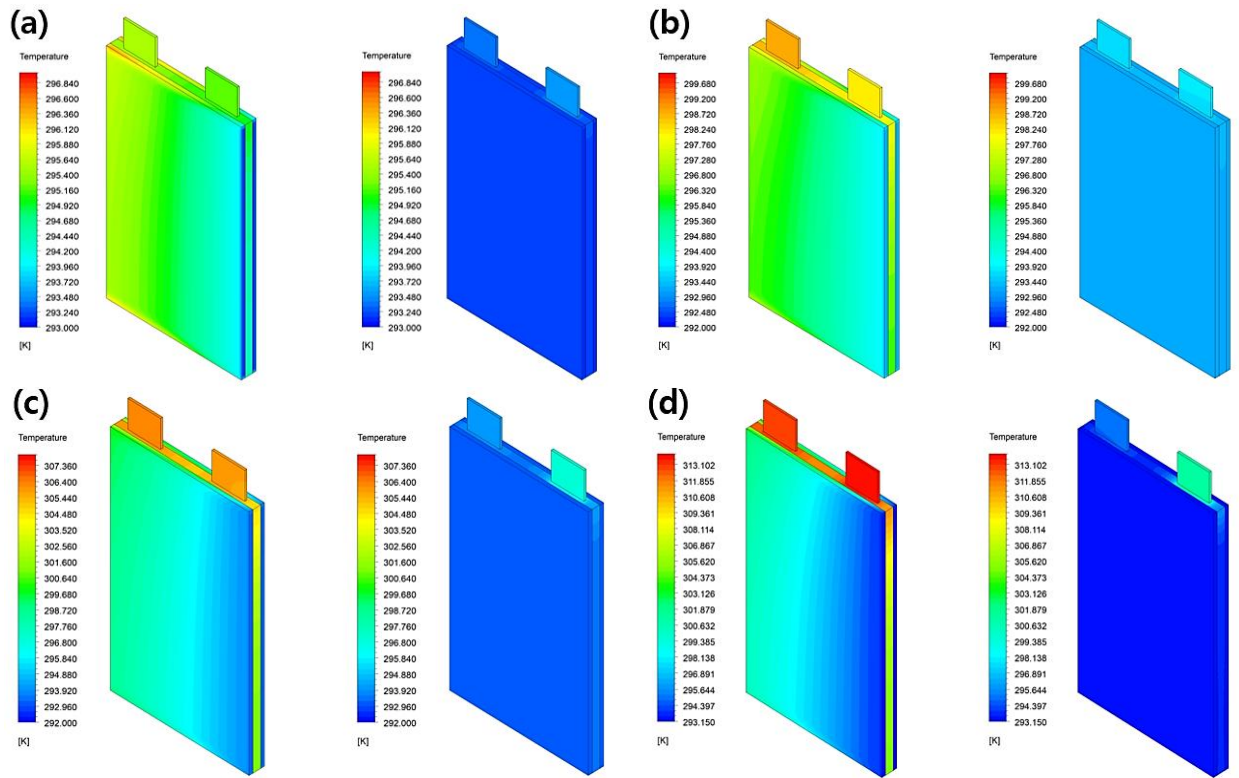
Figure 23. The temperature contours of the prismatic battery cell with air-cooling (left) and water-cooling (right) at (a) 1C rate, (b) 2C rate, (c) 3C rate, and (d) 4C rate.

optimal temperature range at the 1C, 2C, 3C, and 4C discharge rate. To compare the cooling performance between the air-cooling and the water-cooling systems, the temperature contours of the battery models with air-cooling and water-cooling at varying C-rates are obtained in Figure 23. As expected, locations close to negative and positive tabs exhibited the highest temperature. In the air-cooling battery model, the air with the inlet temperature of 20 °C was gradually heated as it flowed downstream due to the decrease in the temperature gradient. Therefore, temperature of the outlet area was higher than that of the inlet area. The water-cooling battery model successfully maintained the operating temperature within the optimal range even at the 4C discharge rate with the uniform temperature distribution throughout the battery cell. It should be noted that unlike the air-cooling battery model, the inlet area exhibited higher temperature than

the outlet area. This is because of the relatively high water inlet velocity of 0.5 m/s: although the air does not show this thermal behavior due to tis low density, for a liquid coolant, such as water, the inlet velocity of 0.5 m/s causes rapid flows of the water, making it difficult to cool down the upstream area in time. In case of a low inlet velocity, in contrast, the upstream area should be cooled down first. Generally, a liquid is a more suitable coolant than the air in terms of the cooling performance. However, other components that need to be incorporated into the system, such as pipes and pumps, can increase the manufacturing cost as well as the size of the battery system. Therefore, although the cooling effect is only considered in this paper, the trade-off relationship should be carefully considered depending on a specific application of a battery system.

6.4) Prismatic Lithium-ion Battery Module

To investigate the thermal behavior of a large-scale Li-ion battery system, a Li-ion battery module in which five battery cells with cold plates are connected in series was developed. The 3D geometry of the 5s (five serially connected batteries in a stage) battery module was built in the DesignModeler, which was further imported to the Mesh (Figure 24). The 5s battery module has a total six cold plates. Each battery cell was sandwiched between two cold plates. Subsequently, in the Mesh, 548,696 nodes and 101,868 elements were generated. The effects of the inlet velocity and temperature of a coolant on the thermal behavior of the 5s battery module were then closely monitored. Other parameters, such as the initial DOD, the operating voltage range, and material properties remained the same. The previously used MSMD battery model and NTGK electrochemical sub-model were also used in this simulation. Boundary conditions also remained unchanged.
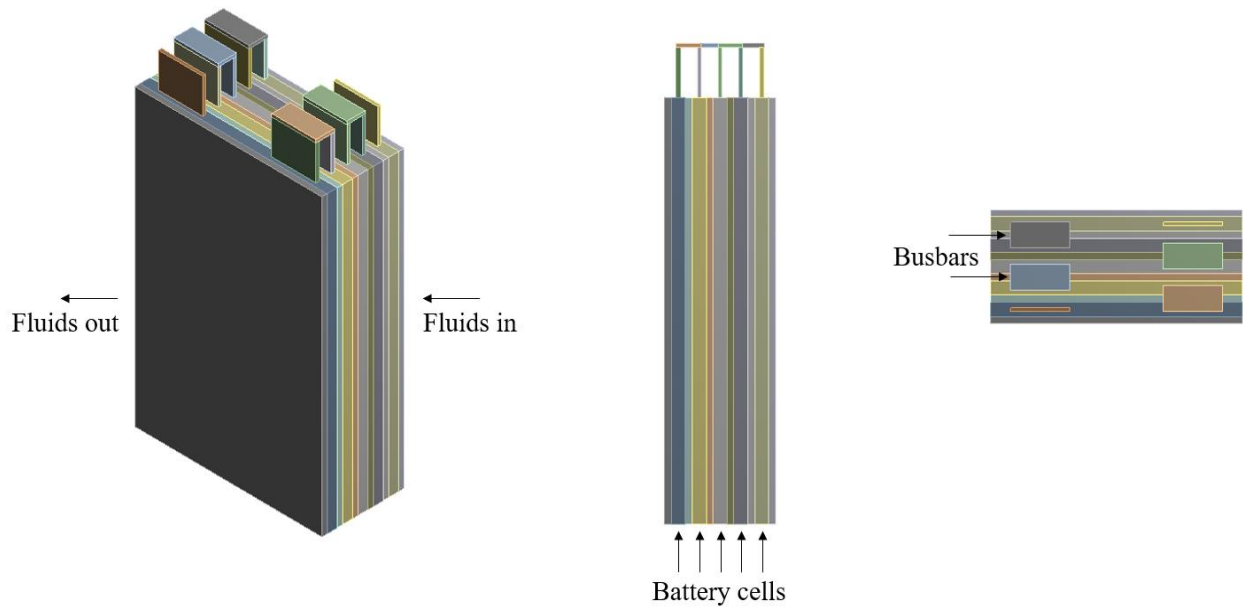
Figure 24. The 3D geometry of the 5s battery module.

6.4.1) Effects of the Inlet Velocity of a Coolant

The thermal response of the 5s battery module was evaluated at different inlet velocities. The air was chosen as a coolant to obtain more distinct temperature variations with the inlet temperature of 20, and velocities of 0.5 m/s, 1 m/s, 1.5 m/s, and 2 m/s were evaluated at the 2C discharge rate. The maximum temperature and the maximum temperature difference, which is described as the difference between the maximum and minimum temperature, of each battery cell in the 5s battery module are shown in Figure 25. As previously demonstrated, cold plates successfully dissipated the heat generated by electrochemical reactions, remaining the maximum temperature of each battery cell in the optimal temperature range. The cell 3 located in the middle of the 5s battery module exhibited the highest temperature throughout the whole simulations. This is because of the sandwiched structure: the temperature of cold plates that sandwich the cell 3 is also affected by the heat conduction from cell 2 and 4. Similarly, the temperature of other intermediate cells, cell 2 and cell 4, was higher than that of the non-

Figure 25. The maximum temperature (T_{max}) and the maximum temperature difference ($T_{max} - T_{min}$) of each battery cell in the 5s battery module.

intermediate cells, cell 1 and cell 5, which were placed at both sides of the 5s battery module. Although the maximum temperatures of all simulation models were in the optimal temperature range, the 5s battery module with the inlet velocities of 0.5 m/s and 1 m/s exhibited the highly non-uniform cell-to-cell temperature distribution. Moreover, the maximum temperature difference in each battery cell was high. Such a temperature imbalance induces a short cycle life and serious safety concerns. The high inlet velocities of 1.5 m/s and 2 m/s mitigated this issue, maintaining the maximum temperature difference between five battery cells within 5 °C. Also, the maximum temperature difference in each battery cell remained within 2 °C. The contours of temperature of the 5s battery module at different inlet velocities are shown in Figure 26. As the inlet velocity increases, the uniform temperature distribution as well as a decrease in the operating temperature were achieved. By simple numerical simulations, it is demonstrated that the coolant velocity significantly affects the cooling effect of a BTMS. Thus, the inlet velocity of
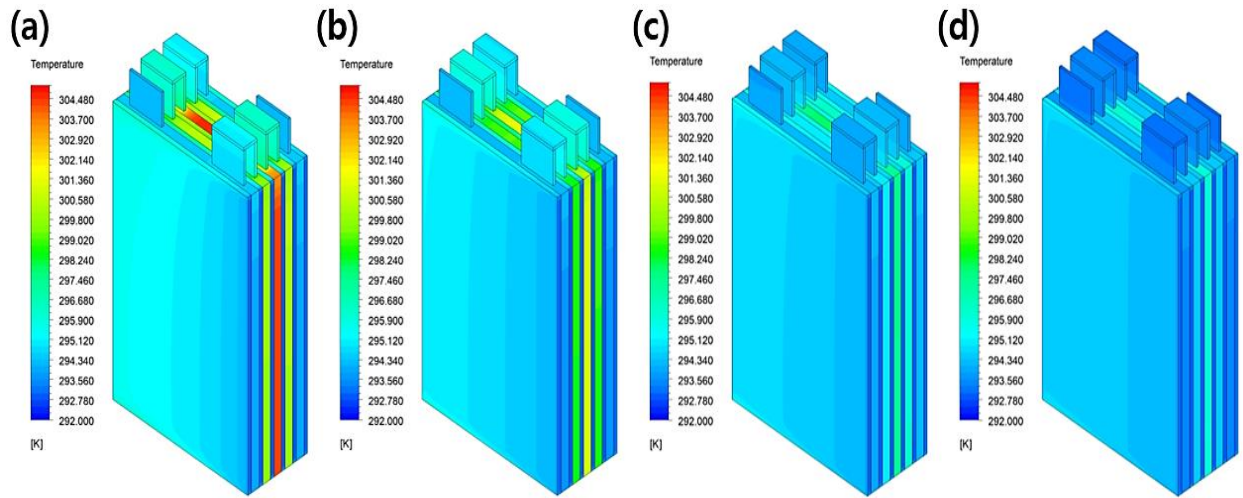
Figure 26. The temperature distribution of the 5s battery module at a coolant velocity of (a) 0.5 m/s, (b) 1 m/s, (c) 1.5 m/s, and (d) 2 m/s.

a coolant must be appropriately chosen depending on a specific application.

6.4.2) Effects of the Inlet Temperature of a Coolant under a Fast Discharging Condition

Heat transfer is mainly affected by three important factors: the thermal conductivity of a heat transfer medium, the temperature gradient, and the amount of contact area between the heat transfer medium and an object. Although the enormous heat generated in a battery module can be dissipated by simply increasing the inlet velocity of a coolant, as confirmed in the previous section, high inlet velocities of a coolant require a high pump power. Therefore, other factors, such as the amount of the contact area and the inlet temperature, should be considered to achieve high cooling performance as well as a reasonable manufacturing cost. In general, fins are used to enhance the cooling performance by substantially increasing the contact area, however, due to cost and space limitations, it is challenging to incorporate fins in each battery cell. Instead, an appropriate selection of the inlet temperature can significantly increase the cooling performance. To gain a deeper insight into the influence of the inlet temperature on the cooling performance,
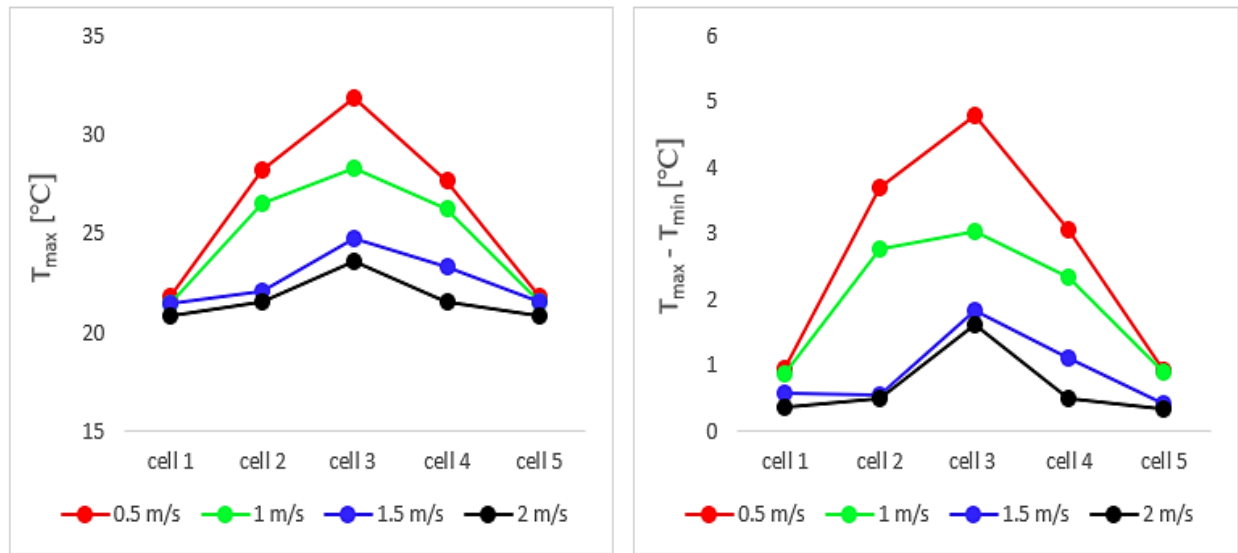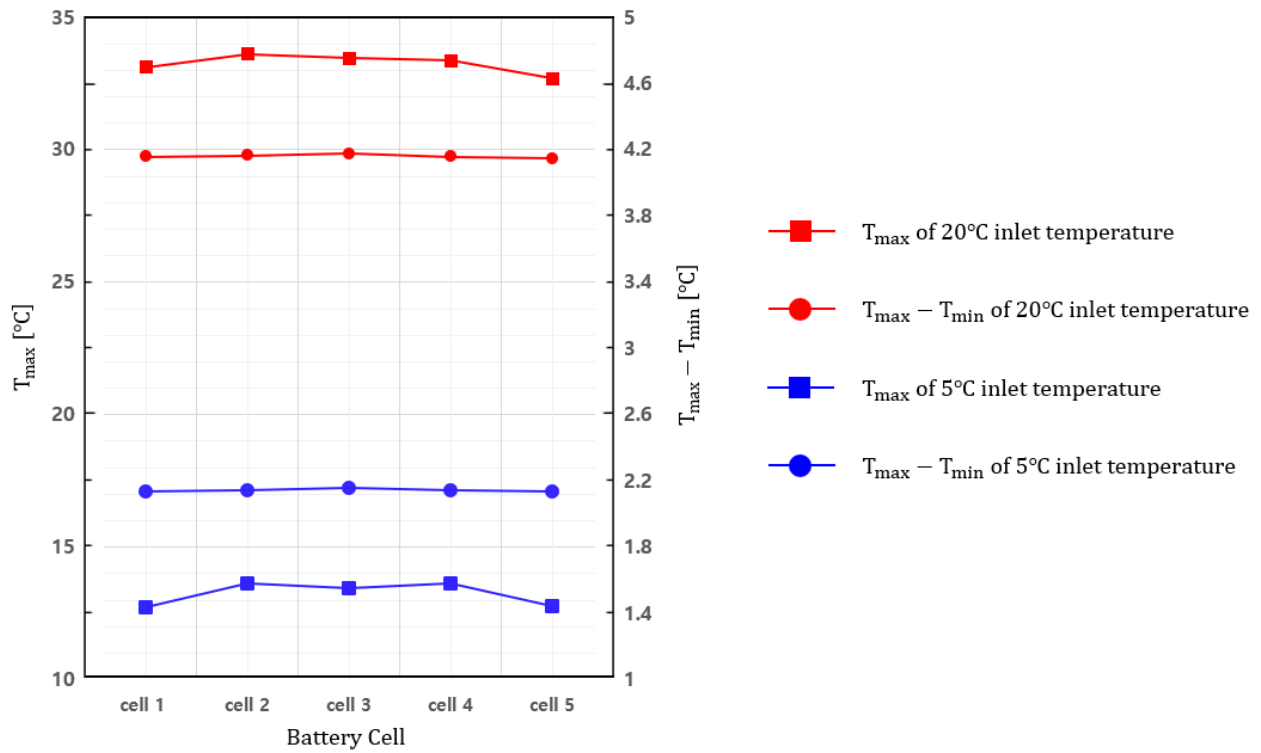
Figure 27. The maximum temperature (T_{max}) and the maximum temperature difference ($T_{max} - T_{min}$) of each battery cell with the inlet temperature of 5 °C and 20 °C.
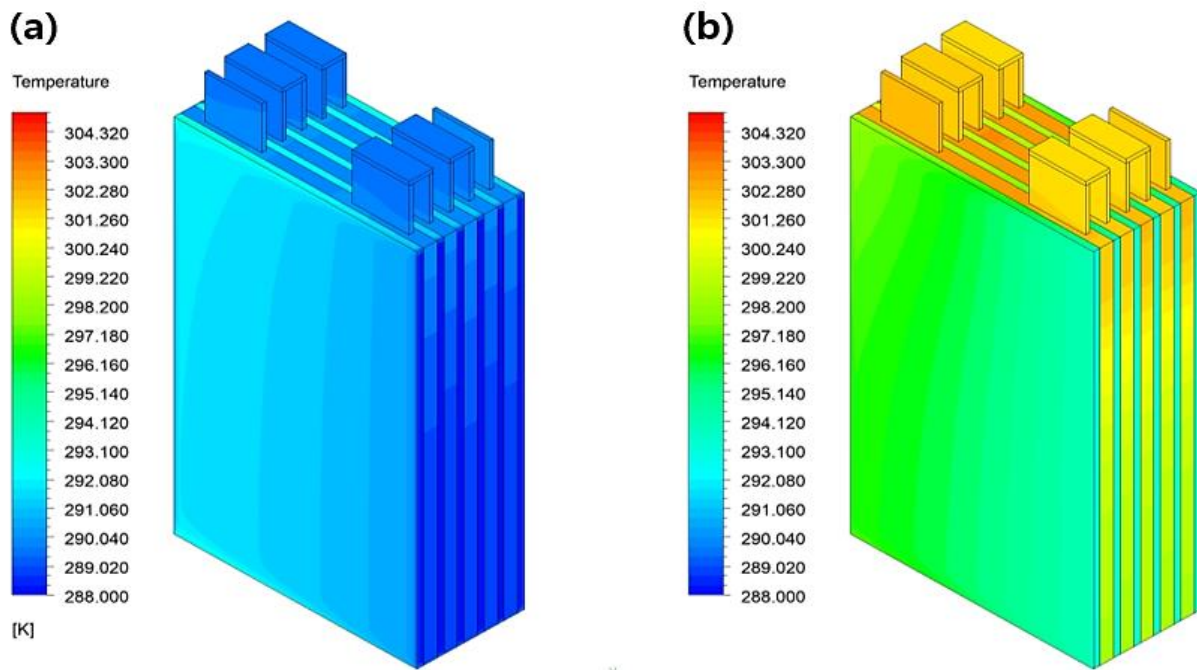
Figure 28. The temperature distribution of the 5s battery module with the inlet temperatures of (a) 5 °C and (b) 20 °C under the 5C fast discharging condition. The inlet velocity was set to 1 m/s.

the 5s battery module with different inlet temperatures under a fast discharging condition was simulated. The air was used as a coolant, and the inlet velocity was set to 1 m/s. The inlet temperatures of 5 °C and 20 °C were chosen in this simulation. The rest of the simulation conditions remained consistent. The battery module was then discharged at the 5C discharge rate. Figure 27 shows the maximum temperature and the maximum temperature difference obtained from the simulation. As discussed before, intermediate cells, cell 2, cell 3, and cell 4, exhibited higher temperature than non-intermediate cells due to the heat conduction from the adjacent battery cells. The inlet temperature of 20 °C was adequate to maintain the operating temperature in the optimal range with the uniform cell-to-cell temperature distribution at the 5C discharge rate. However, the maximum temperature difference was an average of 4.72 °C, which is quite close to 5 °C, the maximum acceptable imbalance in temperature between battery cells. This issue was successfully resolved in the battery model with the inlet temperature of 5 °C. The low inlet temperature successfully cooled down the 5s battery module with a significant improvement in temperature distribution as shown in Figure 28. The maximum temperature difference in each cell was an average of 1.52 °C. In other words, a decrease in the inlet temperature of a coolant enhances the cooling effect as well as the uniformity of the temperature distribution. Therefore, the inlet temperature must be properly chosen with consideration of other critical parameters, for example, the velocity of a coolant and the ambient temperature, depending on a specific application.

6.5) Thermal Design of a Cylindrical Lithium-ion Battery Pack
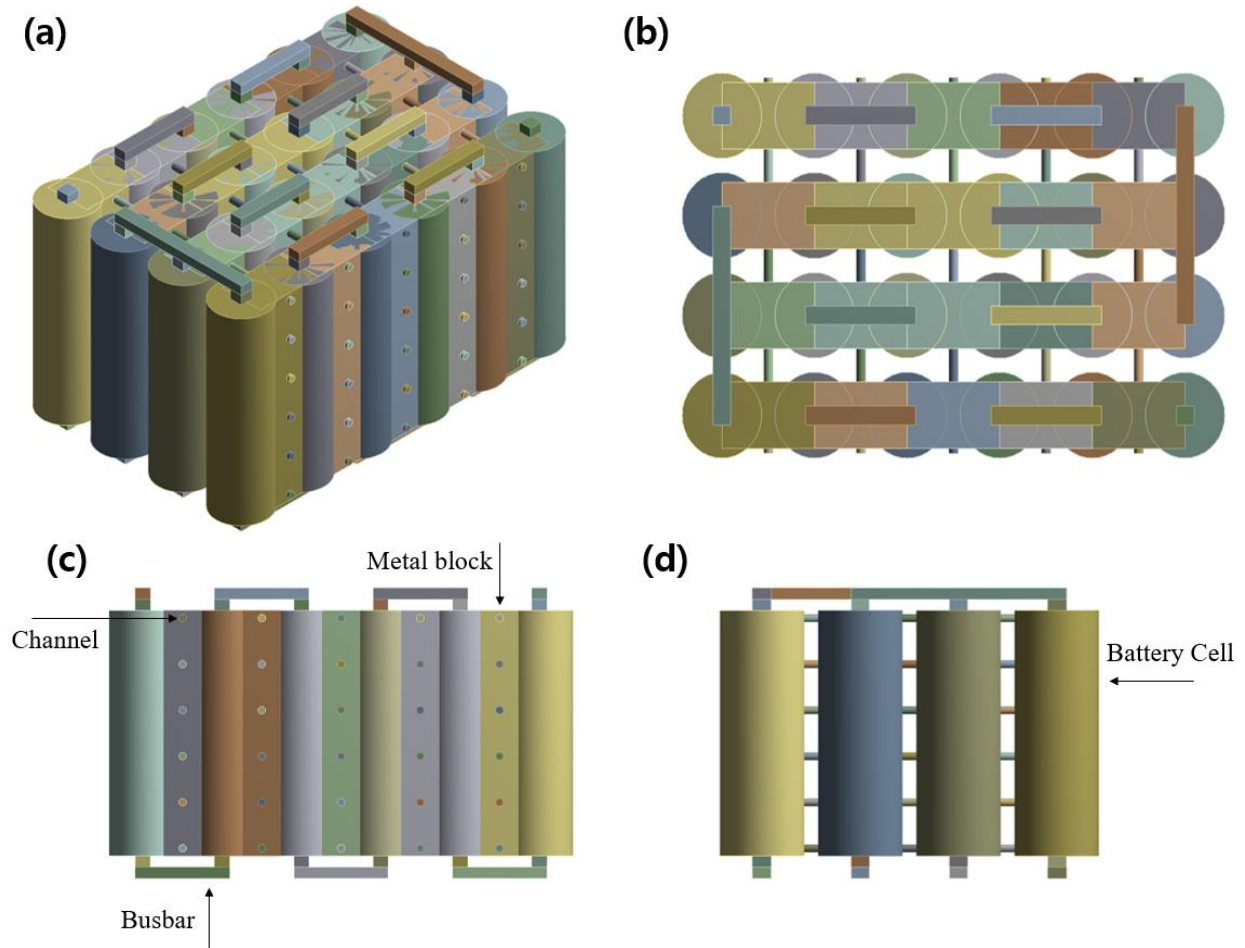
Figure 29. The 3D geometry of the 6s4p battery pack: (a) 3D view, (b) top view, (c) front view, and (d) side view.

Typically, the geometries of a battery cell can be classified into two categories: prismatic and cylindrical configurations. As previously demonstrated, cold plates can efficiently cool down a prismatic Li-ion battery cell. Since the amount of contact area is an imperative factor in heat transfer, a BTMS should be properly designed depending on a configuration of a battery cell. In this section, a 3D thermal design for a cylindrical Li-ion battery pack is presented. Due to the
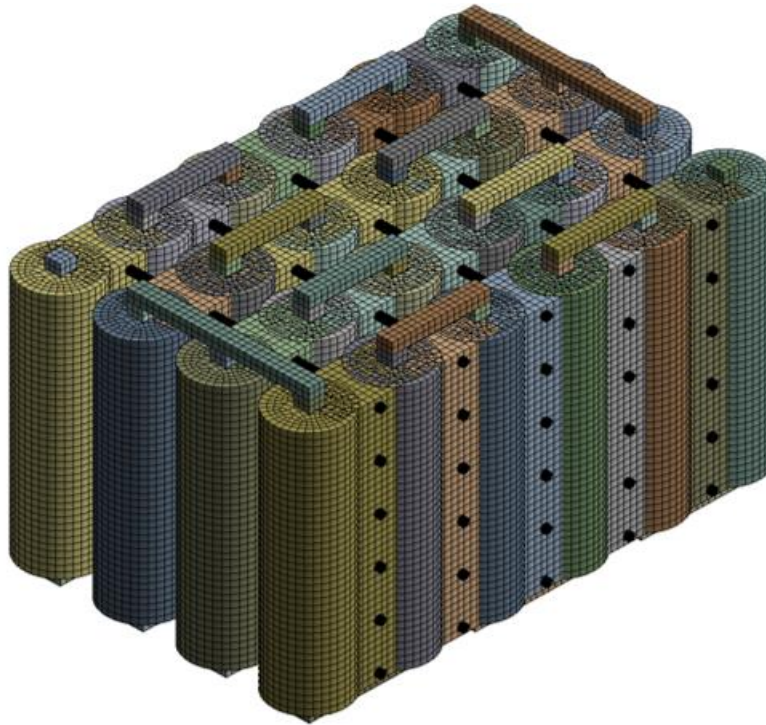
Figure 30. The mesh generated for the 3D 6s4p battery pack. A total 6,664,800 nodes and 1,507,424 elements are generated.

limited simulation capability provided by the ANSYS Fluent student license, simulations did not proceed. The Li-ion battery pack consists of 24 cylindrical cells connected in series and parallel: the 6s4p (6 serial and 4 parallel batteries in a stage) Li-ion battery pack. Such a large-scale battery pack, which is usually incorporated into EVs and HEVs to provide the essential power and energy, must have a proper BTMS during the operation since a slight un-uniformity in temperature distribution can result in a severe imbalance in the cell-to-cell SOH, SOC, and operating temperature, leading to a localized capacity deterioration as well as poor electrochemical performance of the battery system. Since the 6s4p battery pack generates a tremendous amount of heat, a liquid-cooling system is preferred to effectively dissipate the heat. The 3D geometry of BTMS for the 6s4p battery pack was built in the DesignModeler (Figure 29).

Under subsonic conditions, the cross-sectional area is inversely proportional to velocity of a fluid. Therefore, diameter of the cylindrical channels should be small, for example, 2 mm or 2.5 mm, to achieve high cooling effect. Materials used for the metal block should have high thermal conductivity to maximize the cooling performance. Candidates include copper, aluminum, and brass. Although 3D thermal analysis for the 6s4p battery pack is not provided in this section because the number of mesh nodes and elements exceeds the simulation capability supported by the student license (Figure 30), studies on a BTMS for cylindrical Li-ion batteries have been reported elsewhere [90-91].

CHAPTER 7. CONCLUSION & FUTURE WORK

In this thesis, characterization, modeling, and BMS/BTMS for high-performance Li batteries are proposed. State-of-the-art of commercial Li-ion batteries and research efforts to improve the electrochemical performance are first proposed in Chapter 1. The fundamentals of the problematic Li dendritic growth, which hinders the practical applications of the Li metal anode, are then discussed in Chapter 2. In Chapter 3, the phase-field method, a powerful tool to theoretically study the fundamentals of Li dendritic growth, is introduced. The PFM developed by Ely et al. [48] and their simulation results are also proposed to obtain a deeper understanding of formulation and framework of the phase-field method. Finally, in Chapter 4, multi-directional porous Ti nanorods are presented as a solution to achieve the dendrite-free Li metal anode. At the initial Li electrodeposition process, the high level of porosity of the Ti nanorods provided preferential nucleation sites for Li, facilitating Li electro-crystallization on the surface of the nanorods. After the initial Li crystallization, the multi-directional nature of the Ti nanorods further engages lateral Li growth on their body due to low energy cost, resulting in the structural evolution I refer to 'fat nanorods'. As Li plating proceeds, adjacent nanorods covered with Li became physically in contact, eventually forming a smooth layer on the top of the Ti nanorods. As a result, the undesirable Li dendrite formation was completely avoided even after 24 hours of Li electrodeposition. The Ti nanorods significantly improved cell stability and the Coulombic efficiency: the discharge/charge overpotential of ~8 mV and the Coulombic efficiency of 100 %, all of which remained for 1,400 cycles at a current density of 1 mA/cm^2 and a capacity of 1 mAh/cm^2. In Chapter 5, the fundamentals of a BMS is briefly introduced. Furthermore, the 3D thermal analysis of Li-ion batteries is proposed in Chapter 6. The BTMSs built in the ANSYS Fluent used an active cooling system to effectively dissipate the heat generated in Li-ion batteries.

Simulation results showed that the optimal operating temperature and the uniform temperature distribution were achieved by the implementation of the developed BTMSs. The effect of fluid properties on the cooling effect is also studied by using the air and water as a coolant. Simulation results showed that water provides more cooling effect than the air. Moreover, the influences of the inlet velocity and temperature of a coolant are investigated. Although high inlet velocities contributed to an improvement in the cooling performance, the corresponding high-power requirements are not desirable. The low inlet temperature significantly improved the cooling effect as well as the uniformity of the temperature distribution under the 5C fast discharging condition.

Ongoing and future research work includes designs of a BMS with consideration of temperature variations, modeling of advanced thermal control systems for EVs and HEVs, and numerical simulations of Li electrodeposition on the Ti nanorods to study the interface-dependent behavior of Li dendrites.

REFERENCES

1) Deng, D., M. G. Kim, J. Y. Lee and J. Cho (2009). "Green energy storage materials: Nanostructured TiO_2 and Sn-based anodes for lithium-ion batteries." <u>Energy & Environmental Science</u> **2**(8): 818-837.

2) Liu, Q., X. Su, D. Lei, Y. Qin, J. Wen, F. Guo, Y. A. Wu, Y. Rong, R. Kou and X. Xiao (2018). "Approaching the capacity limit of lithium cobalt oxide in lithium ion batteries via lanthanum and aluminium doping." <u>Nature Energy</u> **3**(11): 936-943.

3) Aurbach, D., Y. Talyosef, B. Markovsky, E. Markevich, E. Zinigrad, L. Asraf, J. S. Gnanaraj and H.-J. Kim (2004). "Design of electrolyte solutions for Li and Li-ion batteries: a review." <u>Electrochimica Acta</u> **50**(2-3): 247-254.

4) Li, Z., H. Zhang, P. Zhang, G. Li, Y. Wu and X. Zhou (2008). "Effects of the porous structure on conductivity of nanocomposite polymer electrolyte for lithium ion batteries." <u>Journal of Membrane Science</u> **322**(2): 416-422.

5) Wang, P., S. M. Zakeeruddin, P. Comte, I. Exnar and M. Grätzel (2003). "Gelation of ionic liquid-based electrolytes with silica nanoparticles for quasi-solid-state dye-sensitized solar cells." <u>Journal of the American Chemical Society</u> **125**(5): 1166-1167.

6) Guyomard-Lack, A., J. Abusleme, P. Soudan, B. Lestriez, D. Guyomard and J. L. Bideau (2014). "Hybrid silica–polymer ionogel solid electrolyte with tunable properties." <u>Advanced Energy Materials</u> **4**(8): 1301570.

7) Kim, J. Y., S. K. Kim, S.-J. Lee, S. Y. Lee, H. M. Lee and S. Ahn (2004). "Preparation of micro-porous gel polymer for lithium ion polymer battery." <u>Electrochimica acta</u> **50**(2-3): 363-366.

8) Chen, X., B. Put, A. Sagara, K. Gandrud, M. Murata, J. A. Steele, H. Yabe, T. Hantschel, M. Roeffaers and M. Tomiyama (2020). "Silica gel solid nanocomposite electrolytes with interfacial conductivity promotion exceeding the bulk Li-ion conductivity of the ionic liquid electrolyte filler." Science Advances **6**(2): eaav3400

9) Li, X., J. Tao, D. Hu, M. H. Engelhard, W. Zhao, J.-G. Zhang and W. Xu (2018). "Stability of polymeric separators in lithium metal batteries in a low voltage environment." Journal of Materials Chemistry A **6**(12): 5006-5015.

10) Zhang, S. S. (2007). "A review on the separators of liquid electrolyte Li-ion batteries." Journal of power sources **164**(1): 351-364.

11) Song, M.-K., Y.-T. Kim, J.-Y. Cho, B. W. Cho, B. N. Popov and H.-W. Rhee (2004). "Composite polymer electrolytes reinforced by non-woven fabrics." Journal of Power Sources **125**(1): 10-16.

12) Fang, C., X. Wang and Y. S. Meng (2019). "Key issues hindering a practical lithium-metal anode." Trends in Chemistry.

13) Meng, X. and D. Deng (2015). "Core–Shell Ti@ Si Coaxial Nanorod Arrays Formed Directly on Current Collectors for Lithium-Ion Batteries." ACS applied materials & interfaces **7**(12): 6867-6874.

14) Tarascon, J. and M. Armand (2001). "Issues and challenges facing rechargeable lithium batteries Nature 414."

15) Armand, M. and J.-M. Tarascon (2008). "Building better batteries." nature **451**(7179): 652-657.

16) Evarts, E. E. (2015). "To the limits of lithium." Nature **526**(7575): S93.

17) Choi, J. W. and D. Aurbach (2016). "Promise and reality of post-lithium-ion batteries with high energy densities." Nature Reviews Materials **1**(4): 1-16.

18) Liu, B., J.-G. Zhang and G. Shen (2016). "Pursuing two-dimensional nanomaterials for flexible lithium-ion batteries." Nano Today **11**(1): 82-97.

19) Aurbach, D., M. Daroux, P. Faguy and E. Yeager (1987). "Identification of surface films formed on lithium in propylene carbonate solutions." Journal of The Electrochemical Society **134**(7): 1611.

20) Aurbach, D., Y. Ein-Eli, B. Markovsky, A. Zaban, S. Luski, Y. Carmeli and H. Yamin (1995). "The study of electrolyte solutions based on ethylene and diethyl carbonates for rechargeable Li batteries: II. Graphite electrodes." Journal of The Electrochemical Society **142**(9): 2882.

21) Aurbach, D., Y. Ein-Ely and A. Zaban (1994). "The surface chemistry of lithium electrodes in alkyl carbonate solutions." Journal of The Electrochemical Society **141**(1): L1.

22) Aurbach, D. (2000). "Review of selected electrode–solution interactions which determine the performance of Li and Li ion batteries." Journal of Power Sources **89**(2): 206-218.

23) Cohen, Y. S., Y. Cohen and D. Aurbach (2000). "Micromorphological studies of lithium electrodes in alkyl carbonate solutions using in situ atomic force microscopy." The Journal of Physical Chemistry B **104**(51): 12282-12291.

24) Lin, D., Y. Liu and Y. Cui (2017). "Reviving the lithium metal anode for high-energy batteries." Nature nanotechnology **12**(3): 194.

25) Xu, R., X. Q. Zhang, X. B. Cheng, H. J. Peng, C. Z. Zhao, C. Yan and J. Q. Huang (2018). "Artificial soft–rigid protective layer for dendrite-free lithium metal anode." Advanced Functional Materials **28**(8): 1705838.

26) Chen, K.-H., K. N. Wood, E. Kazyak, W. S. LePage, A. L. Davis, A. J. Sanchez and N. P. Dasgupta (2017). "Dead lithium: mass transport effects on voltage, capacity, and failure of lithium metal anodes." Journal of Materials Chemistry A **5**(23): 11671-11681.

27) Yip, S. (2007). Handbook of materials modeling, Springer Science & Business Media.

28) Moelans, N., B. Blanpain and P. Wollants (2008). "An introduction to phase-field modeling of microstructure evolution." Calphad **32**(2): 268-294.

29) Boettinger, W. J., J. A. Warren, C. Beckermann and A. Karma (2002). "Phase-field simulation of solidification." Annual review of materials research **32**(1): 163-194.

30) Nestler, B., F. Wendler, M. Selzer, B. Stinner and H. Garcke (2008). "Phase-field model for multiphase systems with preserved volume fractions." Physical Review E **78**(1): 011604.

31) Karma, A. (2001). "Phase-field formulation for quantitative modeling of alloy solidification." Physical Review Letters **87**(11): 115701.

32) Qin, R. and E. Wallach (2003). "A phase-field model coupled with a thermodynamic database." Acta materialia **51**(20): 6199-6210.

33) Kobayashi, H., M. Ode, S. G. Kim, W. T. Kim and T. Suzuki (2003). "Phase-field model for solidification of ternary alloys coupled with thermodynamic database." Scripta materialia **48**(6): 689-694.

34) Böttger, B., A. Carré, J. Eiken, G. Schmitz and M. Apel (2009). "Simulation of microstructure formation in technical aluminum alloys using the multiphase-field method." <u>Transactions of the Indian Institute of Metals</u> **62**(4-5): 299-304.

35) Chen, L.-Q. and A. Khachaturyan (1991). "Computer simulation of structural transformations during precipitation of an ordered intermetallic phase." <u>Acta metallurgica et materialia</u> **39**(11): 2533-2551.

36) Wang, Y., D. Banerjee, C. Su and A. Khachaturyan (1998). "Field kinetic model and computer simulation of precipitation of L12 ordered intermetallics from fcc solid solution." <u>Acta materialia</u> **46**(9): 2983-3001.

37) Vaithyanathan, V. (2002). "Phase-field simulations of coherent precipitate morphologies and coarsening kinetics."

38) Zhu, J., Z. Liu, V. Vaithyanathan and L. Chen (2002). "Linking phase-field model to CALPHAD: application to precipitate shape evolution in Ni-base alloys." <u>Scripta Materialia</u> **46**(5): 401-406.

39) Rätz, A. and A. Voigt (2004). "Phase-field model for island dynamics in epitaxial growth." <u>Applicable Analysis</u> **83**(10): 1015-1025.

40) Rätz, A. and A. Voigt (2004). "Various phase-field approximations for epitaxial growth." <u>Journal of crystal growth</u> **266**(1-3): 278-282.

41) Bhate, D. N., A. Kumar and A. F. Bower (2000). "Diffuse interface model for electromigration and stress voiding." <u>Journal of Applied Physics</u> **87**(4): 1712-1721.

42) Mahadevan, M. and R. M. Bradley (1999). "Phase field model of surface electromigration in single crystal metal thin films." Physica D: Nonlinear Phenomena **126**(3-4): 201-213.

43) Kazaryan, A., Y. Wang and B. R. Patton (1999). "Generalized phase field approach for computer simulation of sintering: incorporation of rigid-body motion." Scripta materialia **41**(5): 487-492.

44) Wang, Y. U. (2006). "Computer modeling and simulation of solid-state sintering: A phase field approach." Acta materialia **54**(4): 953-961.

45) Guyer, J. E., W. J. Boettinger, J. A. Warren and G. B. McFadden (2004). "Phase field modeling of electrochemistry. I. Equilibrium." Physical Review E **69**(2): 021603.

46) Guyer, J. E., W. J. Boettinger, J. A. Warren and G. B. McFadden (2004). "Phase field modeling of electrochemistry. II. Kinetics." Physical Review E **69**(2): 021604.

47) Shibuta, Y., Y. Okajima and T. Suzuki (2007). "Phase-field modeling for electrodeposition process." Science and Technology of Advanced Materials **8**(6): 511.

48) Ely, D. R., A. Jana and R. E. García (2014). "Phase field kinetics of lithium electrodeposits." Journal of Power Sources **272**: 581-594.

49) Chen, L., H. W. Zhang, L. Y. Liang, Z. Liu, Y. Qi, P. Lu, J. Chen and L.-Q. Chen (2015). "Modulation of dendritic patterns during electrodeposition: A nonlinear phase-field model." Journal of Power Sources **300**: 376-385.

50) Yurkiv, V., T. Foroozan, A. Ramasubramanian, R. Shahbazian-Yassar and F. Mashayek (2018). "Phase-field modeling of solid electrolyte interface (SEI) influence on Li dendritic behavior." Electrochimica Acta **265**: 609-619.

51) Abyaneh, M. (2018). "Thermodynamics of Homogeneous and Heterogeneous Nucleation in the Context of Electrocrystallization." Journal of The Electrochemical Society **165**(3): D142-D146.

52) Gránásy, L., T. Pusztai, D. Saylor and J. A. Warren (2007). "Phase field theory of heterogeneous crystal nucleation." Physical review letters **98**(3): 035703.

53) Kelton, K., A. L. Greer (2010). "Nucleation in condensed matter: applications in materials and biology." Elsevier.

54) Warren, J. A., T. Pusztai, L. Környei and L. Gránásy (2009). "Phase field approach to heterogeneous crystal nucleation in alloys." Physical Review B **79**(1): 014204.

55) Tóth, G. I., G. Tegze, T. Pusztai and L. Gránásy (2012). "Heterogeneous crystal nucleation: the effect of lattice mismatch." Physical review letters **108**(2): 025502.

56) Zhang, X. Q., X. B. Cheng, X. Chen, C. Yan and Q. Zhang (2017). "Fluoroethylene carbonate additives to render uniform Li deposits in lithium metal batteries." Advanced Functional Materials **27**(10): 1605989.

57) Markevich, E., G. Salitra and D. Aurbach (2017). "Fluoroethylene carbonate as an important component for the formation of an effective solid electrolyte interphase on anodes and cathodes for advanced Li-ion batteries." ACS Energy Letters **2**(6): 1337-1345.

58) Cheng, X.-B., C. Yan, X. Chen, C. Guan, J.-Q. Huang, H.-J. Peng, R. Zhang, S.-T. Yang and Q. Zhang (2017). "Implantable solid electrolyte interphase in lithium-metal batteries." Chem **2**(2): 258-270.

59) Ota, H., K. Shima, M. Ue and J.-i. Yamaki (2004). "Effect of vinylene carbonate as additive to electrolyte for lithium metal anode." Electrochimica Acta **49**(4): 565-572.

60) Qian, J., W. Xu, P. Bhattacharya, M. Engelhard, W. A. Henderson, Y. Zhang and J.-G. Zhang (2015). "Dendrite-free Li deposition using trace-amounts of water as an electrolyte additive." Nano Energy **15**: 135-144.

61) Fua, K. K., Y. Gong, J. Dai, A. Gong, X. Han, Y. Yao, C. Wang, Y. Wang, Y. Chen and C. Yan (2016). "Flexible, Solid-state, Ion-conducting Membrane with 3D Garnet Nanofiber Networks for Lithium Batteries." Proc. Natl. Acad. Sci. USA **113**: 7094-7099.

62) Zhao, C.-Z., X.-Q. Zhang, X.-B. Cheng, R. Zhang, R. Xu, P.-Y. Chen, H.-J. Peng, J.-Q. Huang and Q. Zhang (2017). "An anion-immobilized composite electrolyte for dendrite-free lithium metal anodes." Proceedings of the National Academy of Sciences **114**(42): 11069-11074.

63) Xu, S., D. W. McOwen, C. Wang, L. Zhang, W. Luo, C. Chen, Y. Li, Y. Gong, J. Dai and Y. Kuang (2018). "Three-Dimensional, Solid-State Mixed Electron–Ion Conductive Framework for Lithium Metal Anode." Nano letters **18**(6): 3926-3933.

64) Xin, S., Y. You, S. Wang, H.-C. Gao, Y.-X. Yin and Y.-G. Guo (2017). "Solid-state lithium metal batteries promoted by nanotechnology: progress and prospects." ACS Energy Letters **2**(6): 1385-1394.

65) Zhao, H., D. Lei, Y. B. He, Y. Yuan, Q. Yun, B. Ni, W. Lv, B. Li, Q. H. Yang and F. Kang (2018). "Compact 3D Copper with Uniform Porous Structure Derived by Electrochemical Dealloying as Dendrite-Free Lithium Metal Anode Current Collector." Advanced Energy Materials **8**(19): 1800266.

66) Liu, Y., D. Lin, Z. Liang, J. Zhao, K. Yan and Y. Cui (2016). "Lithium-coated polymeric matrix as a minimum volume-change and dendrite-free lithium metal anode." Nature communications **7**: 10992.

67) Lin, D., Y. Liu, Z. Liang, H.-W. Lee, J. Sun, H. Wang, K. Yan, J. Xie and Y. Cui (2016). "Layered reduced graphene oxide with nanoscale interlayer gaps as a stable host for lithium metal anodes." Nature nanotechnology **11**(7): 626-632.

68) Fan, Y., K. Huang, Q. Zhang, Q. Xiao, X. Wang and X. Chen (2012). "Novel silicon–nickel cone arrays for high performance LIB anodes." Journal of Materials Chemistry **22**(39): 20870-20873.

69) Wang, D., Z. Yang, F. Li, X. Wang, D. Liu, P. Wang and D. He (2011). "Performance of Si–Ni nanorod as anode for Li-ion batteries." Materials Letters **65**(21-22): 3227-3229.

70) Bae, K., G. Kang, S. K. Cho, W. Park, K. Kim and W. J. Padilla (2015). "Flexible thin-film black gold membranes with ultrabroadband plasmonic nanofocusing for efficient solar vapour generation." Nature communications **6**(1): 1-9.

71) Deng, D. (2017). "Transition Metal Oxyfluorides for Next-Generation Rechargeable Batteries." ChemNanoMat **3**(3): 146-159.

72) Guo, R., L. Lu, M. Ouyang and X. Feng (2016). "Mechanism of the entire overdischarge process and overdischarge-induced internal short circuit in lithium-ion batteries." Scientific reports **6**: 30248.

73) Schiffer, Z. J., J. Cannarella and C. B. Arnold (2016). "Strain derivatives for practical charge rate characterization of lithium ion electrodes." Journal of The Electrochemical Society **163**(3): A427-A433.

74) Sommer, L. W., A. Raghavan, P. Kiesel, B. Saha, J. Schwartz, A. Lochbaum, A. Ganguli, C.-J. Bae and M. Alamgir (2015). "Monitoring of intercalation stages in lithium-ion cells over charge-discharge cycles with fiber optic sensors." Journal of The Electrochemical Society **162**(14): A2664-A2669.

75) Dubarry, M., C. Truchot and B. Y. Liaw (2012). "Synthesize battery degradation modes via a diagnostic and prognostic model." Journal of power sources **219**: 204-216.

76) Mohtat, P., S. Lee, J. B. Siegel and A. G. Stefanopoulou (2019). "Towards better estimability of electrode-specific state of health: Decoding the cell expansion." Journal of Power Sources **427**: 101-111.

77) Stroe, D.-I., M. Swierczynski, A.-I. Stroe and S. Knudsen Kær (2016). "Generalized characterization methodology for performance modelling of lithium-ion batteries." Batteries **2**(4): 37.

78) Pesaran, A., S. Santhanagopalan and G. Kim (2013). Addressing the impact of temperature extremes on large format li-ion batteries for vehicle applications (presentation), National Renewable Energy Lab.(NREL), Golden, CO (United States).

79) Babapoor, A., M. Azizi and G. Karimi (2015). "Thermal management of a Li-ion battery using carbon fiber-PCM composites." Applied Thermal Engineering **82**: 281-290.

80) Wang, Z., Z. Zhang, L. Jia and L. Yang (2015). "Paraffin and paraffin/aluminum foam composite phase change material heat storage experimental study based on thermal management of Li-ion battery." Applied Thermal Engineering **78**: 428-436.

81) Mahamud, R. and C. Park (2011). "Reciprocating air flow for Li-ion battery thermal management to improve temperature uniformity." Journal of Power Sources **196**(13): 5685-5696.

82) Fan, L., J. Khodadadi and A. Pesaran (2013). "A parametric study on thermal management of an air-cooled lithium-ion battery module for plug-in hybrid electric vehicles." Journal of Power Sources **238**: 301-312.

83) Jin, L., P. Lee, X. Kong, Y. Fan and S. Chou (2014). "Ultra-thin minichannel LCP for EV battery thermal management." Applied energy **113**: 1786-1794.

84) An, Z., K. Shah, L. Jia and Y. Ma (2019). "A parametric study for optimization of minichannel based battery thermal management system." Applied Thermal Engineering **154**: 593-601.

85) Fathabadi, H. (2014). "High thermal performance lithium-ion battery pack including hybrid active–passive thermal management system for using in hybrid/electric vehicles." Energy **70**: 529-538.

86) Zhang, H., C. Li, R. Zhang, Y. Lin and H. Fang (2020). "Thermal analysis of a 6s4p Lithium-ion battery pack cooled by cold plates based on a multi-domain modeling framework." Applied Thermal Engineering: 115216.

87) Manual, A. F. (2015). ANSYS FLUENT Advanced Add-On Modules Version 16. 2. ANSYS, Inc.

88) Liu, Y., Y. G. Liao and M.-C. Lai (2019). Temperature Distribution on Lithium-Ion Polymer Battery Cell: Experiment and Modeling. 2019 IEEE 90th Vehicular Technology Conference (VTC2019-Fall), IEEE.

89) Xu, X., G. Tong and R. Li (2020). "Numerical study and optimizing on cold plate splitter for lithium battery thermal management system." Applied Thermal Engineering **167**: 114787.

90) Zhao, J., Z. Rao and Y. Li (2015). "Thermal performance of mini-channel liquid cooled cylinder based battery thermal management for cylindrical lithium-ion power battery." Energy conversion and management **103**: 157-165.

91) Zhao, J., Z. Rao, Y. Huo, X. Liu and Y. Li (2015). "Thermal management of cylindrical power battery module for extending the life of new energy electric vehicles." Applied thermal engineering **85**: 33-43.

ABSTRACT

CHARACTERIZATION, MODELING, AND THERMAL MANAGEMENT OF HIGH-PERFORMANCE LITHIUM BATTERIES

by

MINJUN BAE

May 2020

Advisor: Dr. Chin-An Tan & Dr. Da Deng

Major: Mechanical Engineering (electrochemistry)

Degree: Master of Science

Lithium-ion (Li-ion) batteries, as one of the most advanced commercial rechargeable batteries, play a crucial role in modern society as they are extensivelyused in portable electronic devices. Nevertheless, the limited electrochemical performance and poor thermal management systems of Li-ion batteries have hindered the expansion of their future applications. In search of alternative electrode materials to develop a battery with higher electrochemical performance, lithium (Li) metal has attracted much attention as an ideal alternative anode material due to its high specific capacity and lowest redox potential. However, needle-like Li dendritic growth causes severe safety concerns and thus prohibits practical applications of the Li metal anode. Furthermore, the high sensitivity of Li-ion batteries to abusive operations requires a sophisticated battery management system (BMS) as well as a battery thermal management system (BTMS), especially for automobile applications. In this thesis, the fundamentals of Li-ion batteries and common research strategies to enhance the electrochemical performance of Li-ion batteries are first introduced. The challenges of next-generation Li metal batteries, namely the undesirable Li

dendritic growth, is then discussed, followed by introduction of an efficient theoretical model to investigate the fundamentals of Li dendritic growth, the phase-field method (PFM). Black metallic titanium (Ti) foils covered with porous nanorod arrays are proposed as a dendrite-free Li metal anode. The porous Ti nanorod arrays provided numerous heterogeneous nucleation sites, significantly contributing to cycling stability and reversibility: discharge/charge voltage overpotentials of ~8 mV and a Coulombic efficiency of 100 % successfully remained for 1,400 cycles at a current density of 1 mA/cm^2 and a capacity of 1 mAh/cm^2. Furthermore, the black metallic Ti can be potentially used in aerospace and solar industries owing to its outstanding ability to absorb light, mechanical robustness, and high corrosion resistance. After the introduction of the Ti nanorods, common methods to model a proper BMS are discussed. Moreover, BTMSs for large-scale Li-ion batteries were designed and simulated by using the ANSYS Fluent. An active cooling system was incorporated into the BTMSs to successfully dissipate the enormous amount of heat generated in a battery cell and maintain the operating temperature within the optimal temperature range. It was shown that the uniform temperature distribution was also achieved by modulations of the inlet temperature and velocity. This thesis provides a deep insight into characterization, modeling, and thermal managementmethods to improve the electrochemical performance of Li batteries.

AUTOBIOGRAPHICAL STATEMENT

I earned a Bachelor of Science in HVAC (heating, ventilation, and air-conditioning) engineering from Pukyong National University (PKNU) in South Korea. Experiences and knowledge obtained from PKNU allowed me to be a versatile engineer.

In August 2018, after I graduated from PKNU, I came back to Wayne State University to pursue a Master of Science in mechanical engineering. I have joined a materials science and chemical engineering laboratory, which *Dr. Da Deng* is in charge of, since the beginning of my maser's journey. In *Dr. Da Deng*'s laboratory, I have mainly worked on the development of nanomaterials for a negative electrode and a separator that can enhance the electrochemical performance of Li batteries. By completing various projects, I have obtained a tremendous amount of knowledge in Li-ion batteries, material characterization skills, and electrochemical testing techniques.

To obtain a wide range of knowledge, I have also been directed by *Dr. Chin-An Tan* in terms of the computational electrochemistry that could theoretically validate the functionality of nanomaterials that I have developed. By modeling Li electrodeposition kinetics, I have gained a great-depth knowledge in electrochemistry as well as the proficiency in MATLAB.

Having two different advisors has brought me an opportunity to obtain a versatile engineering skillset in Li-ion batteries. The weekly presentations and meetings we have had significantly contributed to my academic accomplishments. Thanks to them, I have been able to learn, grow, and become a better academic researcher.

As I am graduating, my goal is to apply my knowledge I obtained from school on actual industrial projects. I am ready to work, learn, and face new challenges outside the school.